The Journal of Chemical Physics

RESEARCH ARTICLE | FEBRUARY 02 2023

Simulating structured fluids with tensorial viscoelasticity

Carlos Floyd ; Suriyanarayanan Vaikuntanathan ; Aaron R. Dinner

J. Chem. Phys. 158, 054906 (2023)
https://doi.org/10.1063/5.0123470

The Journal of Chemical Physics ARTICLE scitation.org/journal/jcp

Simulating structured fluids with tensorial viscoelasticity

Cite as: J. Chem. Phys. 158, 054906 (2023); doi: 10.1063/5.0123470
Submitted: 30 August 2022 • Accepted: 3 January 2023 •
Published Online: 2 February 2023

Carlos Floyd,[1,2,3] Suriyanarayanan Vaikuntanathan,[1,2,3,a)] and Aaron R. Dinner[1,2,3,a)]

AFFILIATIONS

[1] Chicago Center for Theoretical Chemistry, University of Chicago, Chicago, Illinois 60637, USA
[2] Department of Chemistry, University of Chicago, Chicago, Illinois 60637, USA
[3] James Franck Institute, University of Chicago, Chicago, Illinois 60637, USA

[a)] **Authors to whom correspondence should be addressed:** svaikunt@uchicago.edu and dinner@uchicago.edu

ABSTRACT

We consider an immersed elastic body that is actively driven through a structured fluid by a motor or an external force. The behavior of such a system generally cannot be solved analytically, necessitating the use of numerical methods. However, current numerical methods omit important details of the microscopic structure and dynamics of the fluid, which can modulate the magnitudes and directions of viscoelastic restoring forces. To address this issue, we develop a simulation platform for modeling viscoelastic media with tensorial elasticity. We build on the lattice Boltzmann algorithm and incorporate viscoelastic forces, elastic immersed objects, a microscopic orientation field, and coupling between viscoelasticity and the orientation field. We demonstrate our method by characterizing how the viscoelastic restoring force on a driven immersed object depends on various key parameters as well as the tensorial character of the elastic response. We find that the restoring force depends non-monotonically on the rate of diffusion of the stress and the size of the object. We further show how the restoring force depends on the relative orientation of the microscopic structure and the pulling direction. These results imply that accounting for previously neglected physical features, such as stress diffusion and the microscopic orientation field, can improve the realism of viscoelastic simulations. We discuss possible applications and extensions to the method.

I. INTRODUCTION

When a viscoelastic material responds to an external mechanical perturbation, elasticity gives rise to restoring forces that push the system back toward its unperturbed configuration while viscosity dissipates these forces on a material-dependent timescale.[1,2] These dynamics can be exploited to engineer metamaterials with new functionalities[3] and energy-absorbing media.[4,5] They also underlie a form of memory: canonical viscoelastic systems such as structured fluids—dense solutions of interacting particles, such as colloids, surfactants, or polymers[6]—can adapt their microstructure in response to a shear protocol,[7–9] in some cases "learning" multiple frequencies simultaneously.[7]

Viscoelasticity is also important in biological contexts. A fluid's viscoelastic properties can endow a group of swimming micro-organisms with a collective orientation and even speed enhancements.[10–13] Within cells, the actin cytoskeleton, a dynamic network of semiflexible filaments (polymers), cross-linkers, and motors, enables cells to adapt their structural responses to forces for various physiological functions.[14] The cytoskeleton also governs the motions of vesicles and other objects that are driven through the cytoplasm by molecular motors.[15,16] The viscoelasticity of the cytoplasm has even been shown to guide the positioning of the mitotic spindle for cell division.[17,18] Experimental protocols measuring the forces on magnetic particles or objects in optical traps are often used to study the viscoelastic response of the cytoplasm and materials assembled from its constituents.[19–22]

If a structured fluid has an anisotropic component, such as a polymeric network like the actin cytoskeleton,[23] then the viscoelastic forces can have both orientation and timescale dependent characteristics. Quantitatively describing these characteristics is important for understanding dynamics in such a medium and interpreting experiments that probe them. However, existing theoretical treatments are typically limited to isotropic fluids, neglecting the spatial variation of

microscopic distributions over the solvated molecule's orientations. Theoretical treatments of anisotropic structured fluids of which we are aware[24,25] consider only the fluid and thus are not sufficient by themselves to model the dynamics of immersed objects, such as the mitotic spindle, vesicles, or probe particles mentioned above.

Several mathematical treatments of the stochastic dynamics of a Brownian particle immersed in a viscoelastic medium have been extended to account for confining potentials that bias the particle's motion.[26–29] However, these studies focus only on the position of the particle itself and do not allow one to spatially resolve the motion of the surrounding medium, which in the cytoplasm for instance can include nontrivial flow patterns.[17] To resolve an immersed body together with its surrounding medium, it is necessary to use numerical methods to solve the Navier–Stokes equation. Although techniques have been introduced to address various aspects of this problem, they have not previously been integrated to treat the response of a structured fluid with a spatially varying tensorial response (e.g., due to colloidal or polymeric orientation) to the movement of an immersed body. Such a tensorial response can allow for structural memory effects, in which the history of applied stress on, e.g., a polymer network like the actin cytoskeleton creates anisotropic mechanical compliance and even mechanical hysteresis.[9]

In this work, we adapt a tensorial model for viscoelasticity with an explicit microscopic orientation field[25] such that it can be simulated efficiently, and we marry it with the lattice Boltzmann (LB)[30] and immersed boundary (IB)[31–34] approaches to create detailed simulations of an elastic body being driven through a structured fluid. We demonstrate this framework's use for studying physical effects that were previously neglected in hydrodynamic simulations, such as the dependence of viscoelastic return on stress diffusion and the contribution of the underlying orientation field to the elastic response. This framework can be applied in future works to investigate the interplay between viscoelastic restoring forces, driven immersed objects, and the dynamics of molecular orientations.

II. METHODS

In Sec. II A, we briefly summarize the lattice Boltzmann (LB) and immersed boundary (IB) methods, which serve as the foundation of our approach, and we provide further details in Appendix A. As a first step toward simulating viscoelastic fluids, we consider in Sec. II B how to incorporate a scalar model of viscoelasticity into the IB-LB framework. In other words, here we first assume that elastic effects can be adequately captured by the scalar quantity C representing the elastic modulus. The methods presented in Sec. II B have been developed in previous work,[38–43] and they form the basis for our treatment of tensorial elasticity in Sec. II C. There, we generalize the model to allow the elastic modulus to be a rank-four tensor $\mathbf{C}(\mathbf{P})$ that depends on the local mean orientation $\mathbf{P}(\mathbf{r})$ of an explicitly tracked polymer field. For concreteness, in this paper we refer to the viscoelastic medium as being "polymeric," but our methods encompass other structured fluids such as solutions of anisotropic colloids or worm-like micelles.

A. Immersed boundary-lattice Boltzmann method

We represent a fluid by its local mass density $\rho(\mathbf{r},t)$ and velocity $\mathbf{v}(\mathbf{r},t)$ evolving according to

$$\partial_t \rho + \partial_i(\rho v_i) = 0, \tag{1}$$

$$\rho D_t v_i = -\partial_i p + \partial_j \sigma_{ij}^{\mathrm{v}} + f_i. \tag{2}$$

In these equations, ∂_t is a partial derivative with respect to time, $D_t = \partial_t + v_k\partial_k$ is the material derivative, p is the hydrostatic pressure, $\sigma_{ij}^{\mathrm{v}} = \eta_{\mathrm{s}}(\partial_i v_j + \partial_j v_i)$ is the viscous stress tensor, η_{s} is the fluid's dynamic viscosity, and f_i is a body force density, which in later sections encompasses additional aspects of the system's physics. The indices i and j correspond to Cartesian directions and repeated indices imply summation. Equation (1) represents conservation of mass and Eq. (2) is the Navier–Stokes equation.

The standard LB method is a versatile approach to computational fluid dynamics that numerically solves Eqs. (1) and (2). For many systems of interest, it has practical advantages over alternative methods, such as molecular dynamics, lattice gas models, finite element methods, and dissipative particle dynamics.[30] These advantages include comparative ease of implementation, high computational efficiency for many systems, flexibility in handling complex boundary geometries and conditions, ability to handle multicomponent and multiphase flows, and a strong physical basis rooted in the Boltzmann equation.[35]

The LB method represents a fluid on a regular grid with spacing Δx in terms of its phase space distribution. The macroscopic density $\rho(\mathbf{r},t)$ and velocity $\mathbf{v}(\mathbf{r},t)$ are

$$\rho(\mathbf{r},t) = \sum_{n=1}^{N_{LB}} h_n(\mathbf{r},t), \tag{3}$$

$$\rho(\mathbf{r},t)\mathbf{v}(\mathbf{r},t) = \sum_{n=1}^{N_{LB}} \mathbf{c}_n h_n(\mathbf{r},t). \tag{4}$$

The quantities $h_n(\mathbf{r},t), n = 1,\ldots,N_{LB}$, denote fluid distribution functions at position $\mathbf{r}$ and time t. The N_{LB} fixed vectors $\{\mathbf{c}_n\}_{n=1}^{N_{LB}}$ form a discrete set onto which the velocity part of the distribution function is expanded. The choice of N_{LB} vectors, along with the system dimensionality d, define the basic lattice structure of the simulation. In this paper, we take $d = 2$ and $N_{LB} = 9$, the so-called $d2Q9$ lattice.

To simulate the fluid's dynamics, one iterates between collision and streaming steps. In the collision steps, the distribution functions $h_n(\mathbf{r},t)$ at each node are relaxed toward their local equilibrium values to represent the redistribution of fluid velocities. In the streaming steps, the distribution functions are propagated along their corresponding velocity vector $\mathbf{c}_n$ to represent the motion of that fluid population to a neighboring node. The combined collision and streaming step can be expressed as

$$h_n(\mathbf{r}+\mathbf{c}_n\Delta t, t+\Delta t) - h_n(\mathbf{r},t) = \mathscr{C}_n(\mathbf{r},t), \tag{5}$$

where Δt is the simulation time step and $\mathscr{C}_n(\mathbf{r},t)$ is the collision operator. The commonly used Bhatnagar–Gross–Krook form for this operator is

$$\mathscr{C}_n(\mathbf{r},t) = -\frac{\Delta t}{\tau}\left(h_n(\mathbf{r},t) - h_n^{\mathrm{eq}}(\mathbf{r},t)\right), \tag{6}$$

where τ is the relaxation time, which is related to the kinematic viscosity ν_s and the speed of sound constant for the lattice $c_s = \Delta x/\sqrt{3}\Delta t$ through

$$\nu_s = c_s^2\left(\tau - \frac{\Delta t}{2}\right). \tag{7}$$

In Eq. (6), $h_n^{eq}(\mathbf{r},t)$ is the local equilibrium distribution, which depends on the macroscopic density and velocity in Eqs. (3) and (4). Equation (6) thus couples $h_n(\mathbf{r},t)$ to the remaining $h_m(\mathbf{r},t), m \neq n$. We omit here the expression for $h_n^{eq}(\mathbf{r},t)$, which can be found for instance in Ref. 30. It can be shown via Chapman–Enskog analysis that the "lattice Boltzmann equation," Eq. (5), recovers Eqs. (1) and (2) to second order in the Knudsen number of the fluid.

We note that the LB algorithm introduced here assumes that the fluid is finitely compressible, with an isothermal equation of state for the pressure given by

$$p = c_s^2\rho. \tag{8}$$

Given that the fluid is compressible, there could be a contribution to the viscous stress arising from the divergence of the velocity field in addition to the contribution from the shear viscosity. This bulk viscosity contribution to the stress is, however, not included as a term in Eq. (2), resulting from the particular choice $\eta_B = (2/3)\eta_s$ for the solvent's bulk viscosity coefficient.[30] Variations of the LB algorithm are possible that generalize this choice,[36] but we do not consider these here.

The LB method can be extended to simulate an elastic body interacting with a fluid environment. For this, we use the LB method to treat the hydrodynamics of the fluid and the immersed boundary (IB) method to treat the dynamics of the body.[31–34] In Appendix A, we review the IB-LB method, and we refer the readers to Refs. 30 and 37 for detailed descriptions. The IB method is suited to simulating objects that are deformable and permeable to the fluid, such as an immiscible droplet or vesicle. To simulate rigid and volume excluding objects such as a bead, alternative numerical methods, like a moving hard-wall boundary, need to be used. However, the model of viscoelasticity we present in this work should still be applicable to treating the fluid.

B. Scalar viscoelastic model

Early implementations of scalar viscoelasticity in LB simulations altered the collision operator in Eq. (6) or introduced additional fluid density functions to describe polymer orientations.[38–40] Both of these approaches require substantial modifications to the basic LB algorithm and do not easily accommodate varying the viscoelastic model, which limits flexibility. More recent studies have instead favored introducing viscoelastic effects via an additive contribution $\boldsymbol{\sigma}^p$ to the total stress tensor.[41–43] The divergence of $\boldsymbol{\sigma}^p$ is a force density $f_i^p = \partial_j\sigma_{ij}^p$ that can be included in the force $\mathbf{f}$ appearing in Eq. (2). We incorporate this force in the LB algorithm using the method introduced in Ref. 44. A key benefit of this approach is that it is highly modular, allowing the dynamics of $\boldsymbol{\sigma}^p$ to be specified independently from the underlying LB algorithm.

In the Jeffreys fluid model, which we use here, the solvent and viscoelastic systems act in parallel, which implies that their corresponding forces are added together in Eq. (2).[2] The viscoelastic part is further treated using the Maxwell model, in which the elastic and viscous contributions act in series (Fig. 1). The elastic contribution to the viscoelastic stress is then the same as the viscous contribution, which we denote $\boldsymbol{\sigma}^p$. From linear viscoelasticity theory,[1,2,45]

$$\boldsymbol{\sigma}^p = 2C\boldsymbol{\Lambda}^C = 2\eta_p\boldsymbol{\Psi}^\eta, \tag{9}$$

where C is the elastic modulus and η_p is the polymeric viscosity. The total deformation field $\mathbf{u}(\mathbf{r}) = \mathbf{u}^C(\mathbf{r}) + \mathbf{u}^\eta(\mathbf{r})$ is the sum of the elastic and viscous contributions, and it is related to the velocity field by $\mathbf{v}(\mathbf{r}) = \partial_t\mathbf{u}(\mathbf{r})$. The symmetrized deformation and velocity gradients appearing in Eq. (9) are $\Lambda_{ij}^C = \frac{1}{2}\left(\partial_i u_j^C + \partial_j u_i^C\right)$ and $\Psi_{ij}^\eta = \frac{1}{2}\left(\partial_i v_j^\eta + \partial_j v_i^\eta\right)$. We further have $\boldsymbol{\Psi}^C = \partial_t\boldsymbol{\Lambda}^C$ and $\boldsymbol{\Psi} = \boldsymbol{\Psi}^C + \boldsymbol{\Psi}^\eta$, allowing us to write

$$\partial_t\sigma_{ij}^p = 2C\Psi_{ij} - \frac{C}{\eta_p}\sigma_{ij}^p. \tag{10}$$

This last equation is of the desired form for implementation, as it relates the total polymeric stress $\boldsymbol{\sigma}^p$ to the total strain rate tensor $\boldsymbol{\Psi}$, both of which are tracked in simulation.

As a final step, we promote the partial derivative ∂_t to an operator $\mathscr{D}_t$ that is materially objective, in the sense that rigid transformations of the coordinate system leave the dynamical equation unchanged.[1,2,45] Here, we use the corotational (or Jaumann) derivative whose action on a tensor $\mathbf{X}$ is

$$\mathscr{D}_t X_{ij} = D_t X_{ij} + \Omega_{ik}X_{kj} - X_{ik}\Omega_{kj}, \tag{11}$$

where

$$\Omega_{ij} = \frac{1}{2}(\partial_i v_j - \partial_j v_i) \tag{12}$$

represents the local vorticity. Using the corotational derivative in Eq. (10) yields the Johnson–Segalman model.[46,47] An important feature of spatially extended viscoelastic materials is the diffusion of the stress $\boldsymbol{\sigma}^p$ throughout the system volume.[48,49] This effect is captured in the diffusive Johnson–Segalman model[47] described by

$$\mathscr{D}_t\sigma_{ij}^p = 2C\Psi_{ij} - \frac{C}{\eta_p}\sigma_{ij}^p + D_p\partial_{kk}\sigma_{ij}^p, \tag{13}$$

where ∂_{kk} represents the Laplacian operator and D_p is a diffusion constant describing the spreading of stress sustained by the viscoelastic medium. We note that this diffusive term can improve

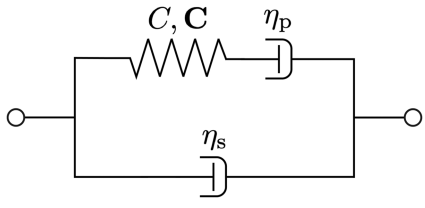

FIG. 1. Circuit diagram of the viscoelastic model used for simulation. The polymeric elasticity is treated either through a scalar elasticity modulus (C) or an elasticity tensor ($\mathbf{C}$). The polymeric elasticity acts in series with the polymeric viscosity (η_p), and together, they act in parallel with the solvent viscosity (η_s).

model stability in some contexts by reducing gradients in the polymeric stress.[43,50,51] We show later that the viscoelastic return of a dragged droplet depends non-monotonically on D_p.

To numerically integrate Eq. (13), we use a finite difference predictor–corrector scheme with the same time step Δt as the LB algorithm. Specifically, we implement Heun's method, also known as the improved Euler method.[85] The viscoelastic stress tensor is defined on the same fixed grid as the fluid velocity and density. This scheme—in which additional physical fields are integrated via finite difference in tandem with the LB algorithm—is known as a hybrid lattice Boltzmann scheme.[52,53] The algorithm described here is schematically illustrated in Fig. 2. In Sec. II C, we use a similar hybrid scheme to track the evolution of a polymeric orientation field $\mathbf{P}(\mathbf{r})$, allowing us to progress beyond the scalar viscoelasticity presented here into a new class of models in which the viscoelastic forces throughout the fluid depend on the local polymer orientation through an elasticity tensor $\mathbf{C}(\mathbf{P})$.

C. Tensorial viscoelastic model

Because the viscoelastic properties of a structured fluid can depend on the local configuration of solvated polymers, we extend the hydrodynamic description of the system to account for the polymer orientation dynamics. Our model of the dynamics builds on previous work on the hydrodynamics of polar gels.[53–55] A common focus of this literature is on active polymer gels, which contain additional contributions to the stress tensor arising from chemical energy consumption. Although our theory could be extended to include these contributions, we omit them here in order to focus on the tensorial character of the local elasticity and how the stiffness tensor depends on the polymer orientation, which were not treated previously.

1. Polymer field dynamics

In this subsection, we summarize the previously established hydrodynamic equations governing the evolution of the polymer orientation field $\mathbf{P}(\mathbf{r}, t)$, primarily following Ref. 53. We then introduce our model, which allows the elasticity tensor $\mathbf{C}$ to depend on $\mathbf{P}$, and we provide an efficient parameterization for $\mathbf{C}(\mathbf{P})$.

Let $\hat{\mathbf{n}}$ represent a unit vector pointing along a polymer's local tangent. At a coarse-grained level of description in two dimensions, a point $\mathbf{r}$ in space is characterized by a local distribution $g(\hat{\mathbf{n}}; \mathbf{r})$ of $\hat{\mathbf{n}}$ over the unit circle. This distribution has a first moment equal to the local polarization vector

$$P_i(\mathbf{r}) = \int_0^{2\pi} \hat{n}_i g(\hat{\mathbf{n}}; \mathbf{r}) d\theta, \tag{14}$$

where $\hat{\mathbf{n}} = (\cos\theta, \sin\theta)$ is specified by a polar angle θ. In three dimensions, this integral would be taken over the unit sphere and the differential $d\theta$ would be replaced by the differential solid angle. In the hydrodynamic theory, only the local polarization vector $\mathbf{P}(\mathbf{r})$ is tracked, and the full distribution $g(\hat{\mathbf{n}}; \mathbf{r})$ is not known. The magnitude P of the polarization vector varies from 0 to 1 as the local distribution $g(\hat{\mathbf{n}})$ goes from a uniform distribution on the circle to

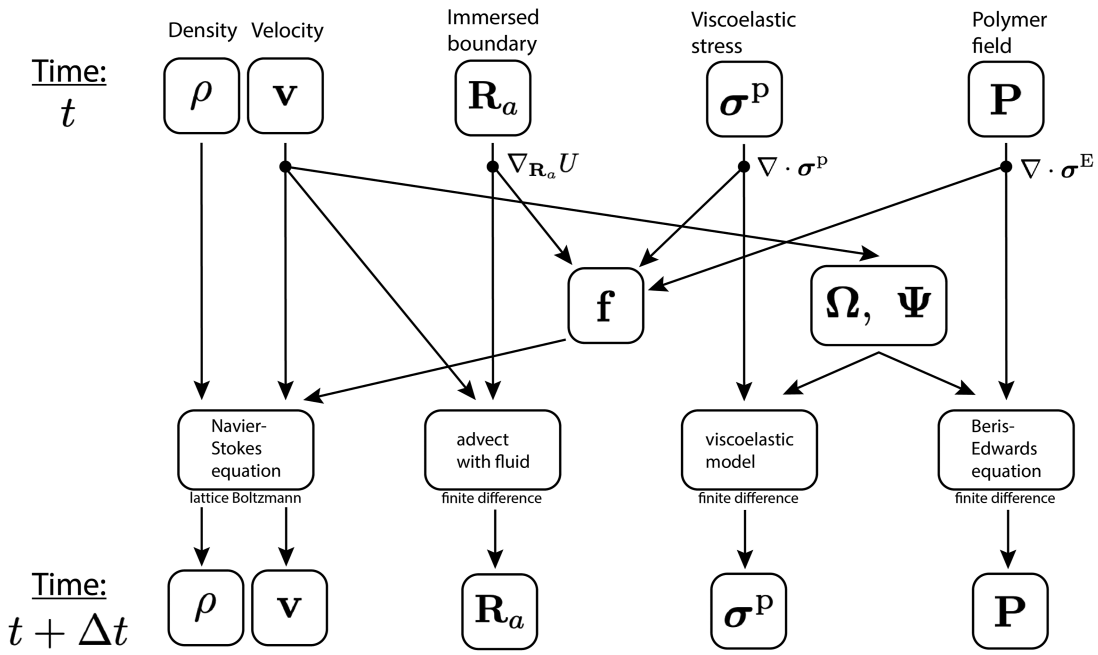

FIG. 2. Simulation flowchart. We show the various fields tracked during simulation and how they influence each other's dynamics as well as the numerical methods used to update the fields from time t to $t + \Delta t$. The fields ρ and $\mathbf{v}$ are updated using the lattice Boltzmann algorithm, whereas the remaining fields $\mathbf{R}_a$, $\boldsymbol{\sigma}^{\mathrm{p}}$, and $\mathbf{P}$ are updated using finite difference methods. A force $\mathbf{f}$ entering into the lattice Boltzmann step takes contributions from three fields, and the field $\mathbf{v}$ in turn influences the dynamics of those three fields both directly and through the tensors $\boldsymbol{\Omega}$ and $\boldsymbol{\Psi}$. Not visualized here is how $\mathbf{P}$ also affects the update of $\boldsymbol{\sigma}^{\mathrm{p}}$ through the stiffness tensor $\mathbf{C}(\mathbf{P})$. Because all fields are updated using inputs from the previous timestep, the order of updates does not matter.

a δ function. The time evolution of field $\mathbf{P}(\mathbf{r},t)$ is governed by the Beris–Edwards equation,[53,56] which for this system takes the form

$$D_t P_i = -\Omega_{ik}P_k + \xi\Psi_{ik}P_k - \Gamma h_i(\mathbf{P}). \tag{15}$$

Here, $\mathbf{\Psi}$ and $\mathbf{\Omega}$ are the symmetric and antisymmetric parts of the velocity gradient tensor $\nabla\mathbf{v}$, ξ is a scalar flow-alignment parameter, Γ is a rotational-diffusion constant, and $\mathbf{h}(\mathbf{P}) = \delta F/\delta\mathbf{P}$ is the molecular field (not to be confused with the fluid population functions h_n in Section II.A), which is derived from a model-specific free energy functional $F[\mathbf{P}]$. In this work, we take $F[\mathbf{P}]$ to be[53,55]

$$F[\mathbf{P}] = \int d\mathbf{r}\left\{\frac{\alpha}{2}|\mathbf{P}|^2 + \frac{\beta}{4}|\mathbf{P}|^4 + \frac{\kappa}{2}(\nabla\mathbf{P})^2\right\}, \tag{16}$$

giving rise to the molecular field

$$h_i(\mathbf{P}) = \left(\alpha + \beta P^2\right)P_i - \kappa\partial_{kk}P_i. \tag{17}$$

The coefficients α and β control the isotropic $(P = 0)$ to polar $(P > 0)$ transition, while κ controls the energetic cost of deformations from the aligned phase. The fluid flow field influences the dynamics of $\mathbf{P}$ via Eq. (15), and $\mathbf{P}$ influences the flow field via an additional contribution to the fluid stress called the Ericksen stress tensor $\boldsymbol{\sigma}^{\mathrm{E}}$, which for this system is[53]

$$\sigma^{\mathrm{E}}_{ij} = -\frac{1}{2}(P_i h_j - h_i P_j) + \frac{\xi}{2}(P_i h_j + h_i P_j) - \partial_i P_k \partial_j P_k. \tag{18}$$

The divergence of this stress tensor is a force density, $f^{\mathrm{E}}_i = \partial_j\sigma^{\mathrm{E}}_{ij}$, which enters on the right-hand side of Eq. (2) and is handled in simulation similarly to other force contributions described earlier. In our hybrid LB implementation, the Beris–Edwards equation is numerically integrated in tandem with the LB algorithm using the predictor–corrector method.

2. Elasticity tensor of the polymer field

Instead of a scalar elasticity modulus C, we now assume that the elastic response to deformation is characterized by a rank-four stiffness tensor $\mathbf{C}$, defined by the relation

$$\sigma^{\mathrm{P}}_{ij} = C_{ijkl}\Lambda^{C}_{kl}, \tag{19}$$

where $\boldsymbol{\sigma}^{\mathrm{P}}$ is the elastic stress tensor experienced in response to a deformation gradient $\mathbf{\Lambda}^{C}$. Incorporating this tensorial element into the Maxwell model, we generalize Eq. (13) as

$$\mathscr{D}_t\sigma^{\mathrm{P}}_{ij} = C_{ijkl}\Psi_{kl} - \frac{1}{2\eta_{\mathrm{P}}}C_{ijkl}\sigma^{\mathrm{P}}_{kl} + D_{\mathrm{P}}\partial_{kk}\sigma^{\mathrm{P}}_{ij}. \tag{20}$$

In principle, the viscous response of the polymers may also require a tensorial description $\eta_{\mathrm{P},ijkl}$, causing the second term in Eq. (20) to depend on a separate tensor formed from the elasticity and viscosity tensors (R_{ijkl} in Ref. 57). This tensor could be straightforwardly accommodated by our model, but we currently neglect it for simplicity.

We next describe how to express the dependence of the stiffness tensor $\mathbf{C}(\mathbf{P})$ on the local polymer polarization vector $\mathbf{P}(\mathbf{r})$. The method presented here is based partly on the work of Kwon and co-workers described in Ref. 25, which itself builds on the work of MacKintosh and co-workers described in Refs. 58–60. The stiffness tensor is expressed as an integral over the local filament orientation distribution as follows:

$$C_{ijkl} = (\rho_{\mathrm{P}} - \rho_{\mathrm{ref}})^a \int_0^{2\pi} g(\hat{\mathbf{n}})K_{ijkl}(\hat{\mathbf{n}})d\theta, \tag{21}$$

where the integral is over the unit circle and $\mathbf{K}$ is a separate rank-four tensor discussed below. The term $(\rho_{\mathrm{P}} - \rho_{\mathrm{ref}})^a$, which depends on the polymer density ρ_{P} and two parameters ρ_{ref} and a, allows for non-affine deformations of the fluid.[25] In the affine case, the expression for $\mathbf{C}$ reduces to the one originally derived by MacKintosh and co-workers as follows:

$$C_{ijkl} = \rho_{\mathrm{P}}K_{\parallel}\int_0^{2\pi} g(\hat{\mathbf{n}})\hat{n}_i\hat{n}_j\hat{n}_k\hat{n}_l d\theta, \tag{22}$$

where $K_{\parallel}$ is the extensional stiffness of the polymer. Thus, in the affine case, $\rho_{\mathrm{ref}} = 0$, $a = 1$, and $K_{ijkl} = K_{\parallel}\hat{n}_i\hat{n}_j\hat{n}_k\hat{n}_l$. The physical basis for Eqs. (21) and (22) is the Irving–Kirkwood formula for the stress tensor, as detailed in Refs. 25, 59, and 61.

The tensor $\mathbf{K}(\hat{\mathbf{n}})$ can be expressed as a rotation of the constant tensor $\mathbf{K}^{\mathrm{x}} = \mathbf{K}(\hat{\mathbf{x}})$ representing the elastic response of cross-linked polymers oriented along the unit vector $\hat{\mathbf{x}}$ in the direction of the x-axis. The nonzero elements of $\mathbf{K}^{\mathrm{x}}$ reflect its material symmetry properties, which we assume here to be transversely isotropic.[25] In this symmetry class, a deformation along $\hat{\mathbf{x}}$ can produce transverse forces in the $\hat{\mathbf{y}}$ direction through non-affine cross-linking of the polymers. To gain insight into the meaning of the elements of $\mathbf{K}^{\mathrm{x}}$, we consider a polymer field oriented purely along the x-axis, so that $\mathbf{C} = (\rho_{\mathrm{P}} - \rho_{\mathrm{ref}})^a\mathbf{K}^{\mathrm{x}}$. We proceed in the Mandel basis, in which rank-four tensors are expressed as matrices in $\mathbb{R}^{3\times3}$ and matrix multiplication is used to represent contraction over multiple indices.[62,63] We denote $\mathbf{K}$ in its Mandel basis as $\widetilde{\mathbf{K}}$ and similarly for other tensors. The constitutive relation for the aligned polymer field is expressed in this basis as [cf. Eq. (19)]

$$\widetilde{\sigma}^{\mathrm{P}}_{\alpha} = (\rho_{\mathrm{P}} - \rho_{\mathrm{ref}})^a\widetilde{K}^{\mathrm{x}}_{\alpha\beta}\widetilde{\Lambda}^{C}_{\beta}, \tag{23}$$

where we use Greek letters as indices in the Mandel basis. Here, $\widetilde{\boldsymbol{\sigma}}^{\mathrm{P}} = (\boldsymbol{\sigma}^{\mathrm{P}}_{11}, \boldsymbol{\sigma}^{\mathrm{P}}_{22}, \sqrt{2}\boldsymbol{\sigma}^{\mathrm{P}}_{12})^{\top}$, $\widetilde{\mathbf{\Lambda}}^{C} = (\mathbf{\Lambda}^{C}_{11}, \mathbf{\Lambda}^{C}_{22}, \sqrt{2}\mathbf{\Lambda}^{C}_{12})^{\top}$, and under the assumption of transverse isotropy, the matrix $\widetilde{\mathbf{K}}^{\mathrm{x}}$ is given as[63]

$$\widetilde{\mathbf{K}}^{\mathrm{x}} = \begin{pmatrix} K^{\mathrm{x}}_{1111} & K^{\mathrm{x}}_{1122} & 0 \\ K^{\mathrm{x}}_{1122} & K^{\mathrm{x}}_{2222} & 0 \\ 0 & 0 & 2K^{\mathrm{x}}_{1212} \end{pmatrix}. \tag{24}$$

In this representation, one can interpret the elements of $\widetilde{\mathbf{K}}^{\mathrm{x}}$ as determining the elastic stress in response to various types of deformations: K^{x}_{1111} is the longitudinal normal stiffness (along $\hat{\mathbf{x}}$) and K^{x}_{2222} is the transverse normal stiffness (along $\hat{\mathbf{y}}$). K^{x}_{1122} represents the reciprocal force generated in one direction in response to a deformation along the orthogonal direction, and K^{x}_{1212} represents an elastic resistance to shearing deformations.

Now, let $\mathbf{T}(\hat{\mathbf{n}})$ be the orthogonal tensor that rotates $\hat{\mathbf{x}}$ to $\hat{\mathbf{n}}$, i.e., $\hat{n}_i = T_{ij}\hat{x}_j$; an expression for $\mathbf{T}(\hat{\mathbf{n}})$ can be obtained in terms of the polar coordinate θ of $\hat{\mathbf{n}}$. With this, $\mathbf{K}(\hat{\mathbf{n}})$ can be written in the original basis as (suppressing the dependence on $\hat{\mathbf{n}}$)

$$K_{ijkl} = T_{iI}T_{jJ}T_{kK}T_{lL}K^{x}_{IJKL} \tag{25}$$

with summation over repeated capital indices implied. The rotation tensor $\mathbf{T}$ and its inverse $\mathbf{T}^{-1}$ have Mandel basis representations $\widetilde{\mathbf{T}}$ and $\widetilde{\mathbf{T}}^{-1}$, for which explicit formulas are available[64] [cf. Eq. (B2)]. In this basis, the rotation in Eq. (25) is equivalent to

$$\widetilde{K}_{\alpha\beta}(\hat{\mathbf{n}}) = \widetilde{T}_{\alpha\gamma}(\hat{\mathbf{n}})\widetilde{K}^{x}_{\gamma\delta}\widetilde{T}^{-1}_{\delta\beta}(\hat{\mathbf{n}}), \tag{26}$$

providing an expression for $\widetilde{\mathbf{K}}(\hat{\mathbf{n}})$ in terms of the elastic constants in $\widetilde{\mathbf{K}}^{x}$ and the orientation of the polymers $\hat{\mathbf{n}}$.

3. Parameterizing the distribution of polymer orientations

We next consider the distribution of polymer orientations, which we now write as a function $g(\theta)$ of the polar angle θ of $\hat{\mathbf{n}}$. Because we track the first moment of this distribution $\mathbf{P}$ in the hydrodynamic model, we wish to find an expression for $g(\theta)$ consistent with $\mathbf{P}$ to use in Eq. (21). We consider the magnitude $P = |\mathbf{P}|$ and orientation $\hat{\mathbf{P}} = \mathbf{P}/P$ separately. We first consider the special case that $\mathbf{P}$ lies along the x-axis (i.e., $\hat{\mathbf{P}} = \hat{\mathbf{x}}$). The polarization P is then obtained from $g(\theta)$ as the mean of the projection along $\hat{\mathbf{x}}$ as follows:

$$P = \int_0^{2\pi} g(\theta)\cos(\theta)d\theta. \tag{27}$$

Viewing Eq. (27) as a constraint on the possible distributions $g(\theta)$, together with the constraint that it is normalized, we now make the physically motivated choice that $g(\theta)$ should maximize the entropy $-\int_0^{2\pi} g(\theta)\ln g(\theta)d\theta$. It can be shown that the unique function with this property is the von-Mises distribution[65] given by

$$g(\theta;k) = \frac{e^{k\cos\theta}}{2\pi I_0(k)}, \tag{28}$$

where $I_0(k)$ is the modified Bessel function of order zero and $k > 0$ is a parameter that determines the anisotropy of the distribution. This function is illustrated in the inset of Fig. 3 for different values of k. To account for the general case when $\hat{\mathbf{P}} \neq \hat{\mathbf{x}}$, we simply find the polar angle θ_P of $\hat{\mathbf{P}}$ and write the density as $g(\theta - \theta_P; k)$.

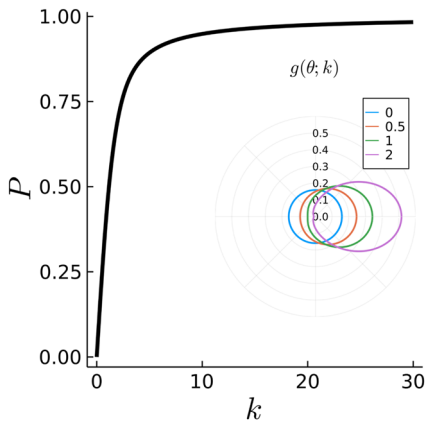

FIG. 3. Plot of the function P in Eq. (29). In the inset, a polar plot of the von-Mises distribution $g(\theta; k)$, Eq. (28), is shown for four values of k ranging from 0 to 2. In the polar plot, the value of $g(\theta; k)$ is represented by the distance from the origin to the curve at the corresponding value of θ.

In addition to its physical motivation, there are two key advantages of this choice for $g(\theta)$. The first is that it allows the integral over θ in Eq. (21) to be performed analytically. The second is that it allows for a one-to-one mapping between P and k, which follows from the relation

$$P(k) = \int_0^{2\pi} g(\theta;k)\cos(\theta)d\theta = \frac{I_1(k)}{I_0(k)}. \tag{29}$$

Although this relation (plotted in Fig. 3) cannot be inverted analytically, k can be readily determined from P numerically. We note that there is no value of k for which $P = 1$, but in practice either the allowed range of P can be restricted to the interval $[0, 1)$, or one can take the limit $k \to \infty$. The equilibrium value of P is determined by the parameters α and β in Eq. (16). In this paper, we ensure

TABLE I. Parameters for droplet pulling simulations.

General parameters	Symbol	Value
Length scale	H_x	4×10^{-8} m
Timescale	H_t	8×10^{-6} s
Density scale	H_ρ	2×10^{7} kg/m^3
Number of steps	N_{steps}	187 500
Collision operator time	τ	1.25
Solvent dynamic viscosity	η_s	0.001 Pa s
Lattice size	N_x, N_y	250, 250
Viscoelastic parameters	**Symbol**	**Value**
Scalar polymeric stiffness	C	0.005 Pa
Polymeric viscosity	η_p	0.05 Pa s
Stress diffusion constant	D_p	10^{-13} m^2/s
Stiffness tensor element[a]	K^{x}_{1111}	0.01 Pa
Stiffness tensor element[a]	K^{x}_{1122}	0.005 Pa
Stiffness tensor element[a]	K^{x}_{2222}	0.005 Pa
Stiffness tensor element[a]	K^{x}_{1212}	0.005 Pa
Beris–Edwards parameters	**Symbol**	**Value**
Flow alignment	ξ	1.1
Polarization coefficients	α, β	−0.9, 1.0
Alignment stiffness	κ	0.001
Rotational-diffusion constant	Γ	1.0
Immersed boundary parameters	**Symbol**	**Value**
IB node distance	l_{eq}	2×10^{-8} m
Droplet radius	R	5×10^{-7} m
Droplet spring stiffness	k_{spring}	10^{-5} N/m
Droplet curvature stiffness	$\varepsilon_{\text{angle}}$	10^{-20} N m
Maximum trap stiffness	k_{trap}	10^{-6} N/m
Droplet pulling distance	d_{pull}	4×10^{-6} m
Droplet pulling time	T_{pull}	0.2 s

[a]For simplicity, the prefactor $(\rho_p - \rho_{\text{ref}})^a$ appearing in Eq. (21) has been absorbed into the values shown here.

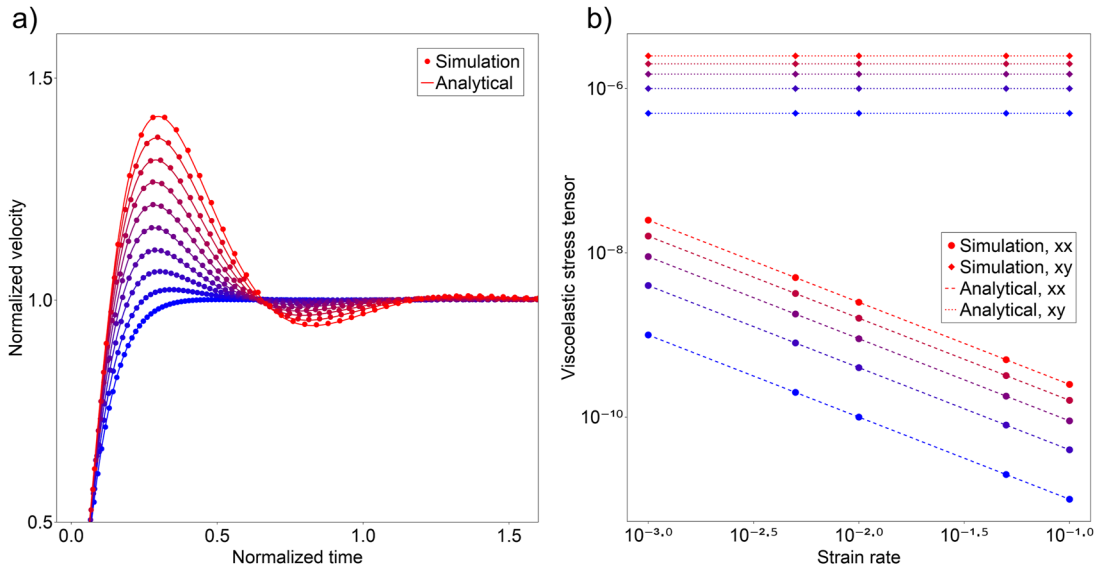

FIG. 4. Validation of the viscoelastic LB implementation against analytically solvable channel flows. (a) The normalized velocity v_x/v_x^N during Poiseuille flow at the channel's midpoint as a function of normalized time t/t_1, where $t_1 = \eta_0/\rho L^2$ and L is the channel height. v_x^N is the steady-state velocity obtained for a Newtonian, i.e., not viscoelastic, fluid. Here, $\lambda_1 = 3000$ and $\eta_s = 1/6$, and we vary η_p from 0.05 to 0.5 in increments of 0.05 while the color ranges from blue to red. The analytical solution to this flow is described in Refs. 66 and 68. (b) The steady-state viscoelastic stress tensor components σ_{xx}^p and σ_{xy}^p during Couette flow. Here, $\eta_p = 0.5$ and C takes the values 0.0005, 0.0025, 0.005, 0.025, and 0.05 as the colors range from blue to red. We simultaneously vary the strain rate $\dot{\gamma} = v_{top}/L$, where v_{top} is the applied velocity at the top of the channel. The analytical solution to this flow is described in Ref. 69. All quantities in this figure are given in lattice units unless noted otherwise, and $L = N_x = N_y = 100$.

through our choices of these parameters that the equilibrium value is less than 1, and we account for the possibility of advection causing $P > 1$ by setting a maximal value $P = 0.99$ when determining k from Eq. (29).

We provide the full expression for $\widetilde{\mathbf{C}}$ obtained using this method in Appendix B. In the isotropic case, when $k = 0$, the expression for $\widetilde{\mathbf{C}}$ reduces to

$$\widetilde{\mathbf{C}} = \begin{pmatrix} \widetilde{C}_{11} & \widetilde{C}_{12} & 0 \\ \widetilde{C}_{12} & \widetilde{C}_{11} & 0 \\ 0 & 0 & \widetilde{C}_{11} - \widetilde{C}_{12} \end{pmatrix}, \tag{30}$$

where

$$\widetilde{C}_{11} = \frac{1}{8}(3K^x_{1111} + 2K^x_{1122} + 4K^x_{1212} + 3K^x_{2222}), \tag{31}$$

$$\widetilde{C}_{12} = \frac{1}{8}(K^x_{1111} + 6K^x_{1122} - 4K^x_{1212} + K^x_{2222}). \tag{32}$$

Equation (30) is the expected isotropic elasticity tensor in the Mandel basis as described in Ref. 63. Equation (30) enters the fluid dynamics through Eq. (19), which can be expressed in terms of the Lamé parameters of an isotropic material as[62]

$$\sigma^p_{ij} = 2\,\mu\Lambda^C_{ij} + \lambda\delta_{ij}\Lambda^C_{kk}, \tag{33}$$

where $\lambda = \widetilde{C}_{12}$ and $\mu = (\widetilde{C}_{11} - \widetilde{C}_{12})/2$ are the first and second Lamé parameters, respectively. The shear modulus of the material is equal to μ, while the bulk modulus is $\lambda + \mu$ in two dimensions. By setting $\widetilde{C}_{12}$ to zero through particular choices of the elements of $\mathbf{K}^x$, a single parameter $\widetilde{C}_{11}$ characterizes the elastic response, and we recover the case of scalar elasticity described in Sec. II B. This simplification of

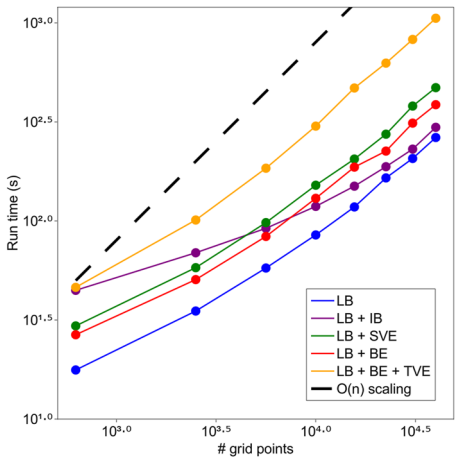

FIG. 5. The simulation run time for five combinations of simulation features plotted as a function of the number of grid points $N_x \times N_y$. In the legend, "LB" refers to the lattice Boltzmann simulator, "IB" refers to the immersed boundary, "SVE" refers to the scalar viscoelastic model without polymers, "BE" refers to the Beris–Edwards dynamics for polymers, and "TVE" refers to tensorial viscoelasticity in which **C** is computed as a function of **P**. The dashed line shows linear scaling of run time with the number of grid points for comparison. These simulations were run serially on single cores of Intel Xeon Gold 6248R processors.

Eq. (30) to a diagonal matrix can be viewed as the reduction to zero of the material's Poisson ratio $\nu = \lambda/(\lambda + 2\,\mu)$ through tuning of λ.

In summary, the local polarization vector $\mathbf{P}(\mathbf{r}) = P\hat{\mathbf{P}}$ determines the stiffness tensor $\widetilde{\mathbf{C}}(\mathbf{P})$ through the orientation parameter θ_P, which depends on $\hat{\mathbf{P}}$, and the anisotropy parameter k, which depends on P. These together specify the parameterized distribution $g(\theta - \theta_P;\, k)$, which enters in the integral in Eq. (21). Given the expression for $\widetilde{\mathbf{K}}(\hat{\mathbf{n}})$ in Eq. (26), the integral can be computed analytically. The result is then used in Eq. (20), which is numerically integrated using a finite difference method as described in Secs. II B and II C.

D. Parameterization

Rheological systems are frequently characterized using several numbers that describe the material properties and the degree of deformation caused by an external force.[1,2,66,67] The material properties are captured by the relaxation time [cf. Eq. (9)] given by

$$\lambda_1 = \frac{\eta_{\mathrm{P}}}{C}, \tag{34}$$

the total viscosity given by

$$\eta_0 = \eta_{\mathrm{P}} + \eta_{\mathrm{s}}, \tag{35}$$

and the dimensionless viscosity fraction given by

$$\beta = \frac{\eta_{\mathrm{P}}}{\eta_0}. \tag{36}$$

Given a time for observing the system T, the dimensionless Deborah number is[1,2,66,67]

$$\mathrm{De} = \frac{\lambda_1}{T}. \tag{37}$$

For $\mathrm{De} \ll 1$, the system flows appreciably over the observation time, while for $\mathrm{De} \gg 1$ the system appears nearly elastic. If the system is driven by an external force, producing a deformation rate U across a system of size L, the strain rate is defined as

$$\dot{\gamma} = \frac{U}{L} \tag{38}$$

and the dimensionless Weissenberg number is

$$\mathrm{Wi} = 2\lambda_1\dot{\gamma}. \tag{39}$$

For $\mathrm{Wi} \gg 1$, the elastic restoring forces far outweigh the viscous forces. Finally, the relative importance of fluid inertia compared to viscous forces is captured by the Reynolds number

$$\mathrm{Re} = \frac{\rho_0 UL}{\eta_0}, \tag{40}$$

where ρ_0 is the typical density of the system.

By working directly in lattice units, these viscoelastic parameters can be prescribed in simulation without setting a physical scale for the system. In other words, the physical length scale H_x, timescale H_t, and density scale H_ρ are all equal to 1. However, to simulate a particular system, it is necessary to fix H_x, H_t, and H_ρ to the scale of the system. To convert physical quantities to lattice units, one divides by the corresponding dimensional combination of these factors.[30]

Our primary application of the methods in this paper is to simulate a lipid droplet being dragged by an optical trap. For this, we followed the general strategy for parameterizing the LB simulations described in Ref. 30. We set the solvent viscosity to that of water, but, following standard practice with LB simulations of microscopic systems, we set the density to several orders of magnitude larger than the density of water.[55,70–72] This allows increasing the time step Δt (thereby accelerating simulations) while ensuring that the system is still in the low Reynolds number regime. To explore their effects, we varied the stress diffusion constant, droplet radius, and pulling time. The default values of these parameters as well as the viscoelastic parameters were chosen to roughly correspond to pulling a small lipid droplet through the cytoplasm.[17] See Appendix A for

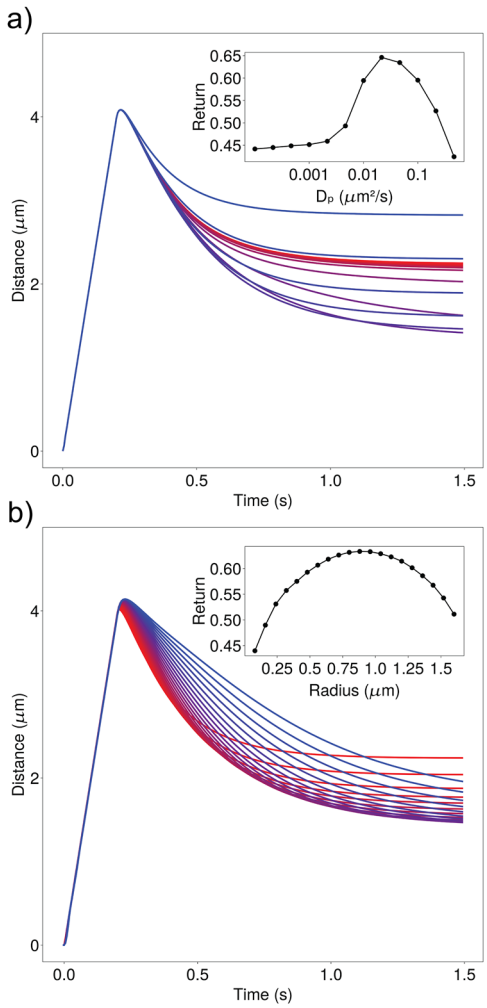

FIG. 6. Distance trajectory for several values of (a) the stress diffusion D_{p} and (b) the droplet radius R. Insets: the value of the return defined in Eq. (42). The color ranges from red to blue in each plot as the parameters increase over the values at which points are plotted in the corresponding insets.

details on the droplet model. The trap stiffness k_{trap} was chosen to be roughly consistent with an optical trap. The droplet's constitutive parameters k_{spring} and $\varepsilon_{\text{angle}}$ were chosen to give appreciable resistance to deformation while remaining numerically stable. The Beris–Edwards parameters are mostly based on previous studies.[55] The parameter values used for all simulations, unless otherwise specified, are given in Table I.

E. Boundary conditions

Several fields make up the system described in this paper, including ρ, $\mathbf{v}$, $\{\mathbf{R}_a\}_{a=1}^{N_{IB}}$, $\boldsymbol{\sigma}^{\text{p}}$, and $\mathbf{P}$, and each requires specifying boundary conditions at the edge of the simulation volume. The fields ρ and $\mathbf{v}$ are handled by the LB algorithm (see Fig. 2) and typically have either periodic or Dirichlet boundary conditions, though Neumann boundary conditions are also possible. In this paper, we implement Dirichlet boundary conditions through the bounce-back method, described in detail in Ref. 30. Through an extension of the bounce-back method, walls can be given a nonzero velocity, which allows simulating shear flow. The IB points $\mathbf{R}_a$ are not prescribed boundary conditions in this work; we simply ensure that these points do not cross the boundary during simulation. The remaining fields $\boldsymbol{\sigma}^{\text{p}}$ and $\mathbf{P}$ are given either periodic or Neumann boundary conditions with zero derivative at the boundary, though it would be straightforward to use Dirichlet or Robin boundary conditions for these fields as well.[73]

F. Validation and performance

We validate the scalar viscoelasticity simulation on two types of channel flow, in which periodic boundary conditions are applied in the x direction and reflecting (i.e., hard-wall) conditions are applied

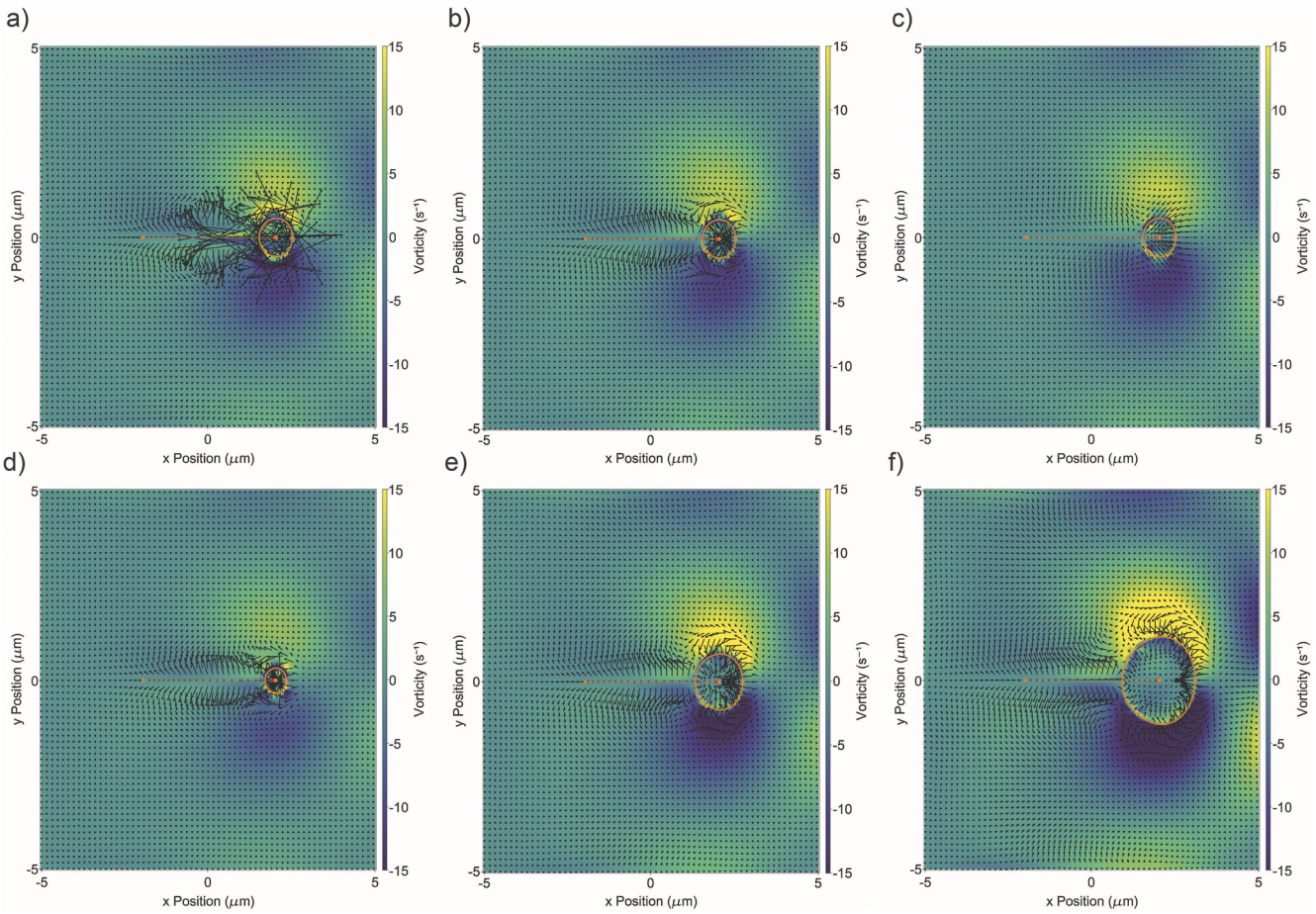

FIG. 7. Example responses to a driven body. Simulations with (a) $D_{\text{p}} = 0.001\ \mu\text{m}^2/\text{s}$ and $R = 0.5\ \mu\text{m}$, (b) $D_{\text{p}} = 0.1\ \mu\text{m}^2/\text{s}$ and $R = 0.5\ \mu\text{m}$, (c) $D_{\text{p}} = 1\ \mu\text{m}^2/\text{s}$ and $R = 0.5\ \mu\text{m}$, (d) $D_{\text{p}} = 0.1\ \mu\text{m}^2/\text{s}$ and $R = 0.32\ \mu\text{m}$, (e) $D_{\text{p}} = 0.1\ \mu\text{m}^2/\text{s}$ and $R = 0.72\ \mu\text{m}$, and (f) $D_{\text{p}} = 0.1\ \mu\text{m}^2/\text{s}$ and $R = 1.12\ \mu\text{m}$. In these images, the color represents the local vorticity of the fluid flow field $\partial_x v_y - \partial_y v_x$, and the arrows, shown at 1/16th of the grid points, are proportional to the local vector $\nabla \cdot \boldsymbol{\sigma}^{\text{p}}$, which represents the viscoelastic restoring force at each point. The thick orange curve represents the boundary of the droplet, defined by the points $\{\mathbf{R}_a\}_{a=1}^{N_{IB}}$ (cf. Fig. 13), and the three orange dots represent the initial center of mass, the current center of mass, and the position of a fixed point on the boundary. The thin orange line traces the trajectory of the center of mass during the pulling protocol. The red dot (which overlaps with the current center of mass) represents the location of the harmonic trap. All snapshots correspond to the time $t = 0.2$ s. Multimedia views: (a) https://doi.org/10.1063/5.0123470.1; (c) https://doi.org/10.1063/5.0123470.2; (d) https://doi.org/10.1063/5.0123470.3; (f) https://doi.org/10.1063/5.0123470.4

in the y direction. In Poiseuille flow, a spatially uniform external force in the x direction is applied to the fluid to capture the effect of a fixed pressure gradient across the channel, and in Couette flow the top boundary at $y = L$ moves with a fixed speed to shear the fluid. Analytical solutions[66,68,69] of both flows exist for an Oldroyd-B fluid, which is the fluid described in Eq. (13) upon setting $D_p = 0$ and replacing the corotational material derivative $\mathscr{D}_t$ with the upper-convected material derivative, whose action on a tensor $\mathbf{X}$ is

$$\mathscr{D}_t^{uc} X_{ij} = D_t X_{ij} - (\partial_k v_i) X_{kj} - (\partial_k v_j) X_{ik}. \tag{41}$$

The analytical solutions apply to incompressible fluids, whereas our implementation assumes a finitely compressible fluid, but we ensure that the density variations are sufficiently small when comparing results. In both cases, we find excellent agreement between simulation and the analytical results as illustrated in Fig. 4. We further validated our simulation of the Beris–Edwards dynamics by measuring the steady-state angle made by the polymer field with respect to the shear flow direction. These results also agree with analytical expressions[74] (results not shown).

We implemented the methods described in this paper in custom Julia[75] code. Although the LB algorithm is amenable to parallelization we did not pursue this here. To evaluate the contribution of the different components of the algorithm to the total run time, we ran simulations of Couette flow with different combinations of features. For each combination, we fixed $N_y = N_x$ and $N_{steps} = 10\,000$ and varied N_x. The results indicate an approximately asymptotic linear scaling of the run time with the system size (slopes of the curves in Fig. 5). In terms of absolute computation time, the cost for the tensorial viscoelasticity is comparable to the sum of the cost for the scalar viscoelasticity and that for the Beris–Edwards dynamics for the polymers. Much of the computational expense for the tensorial model is due to evaluating the tensor $\mathbf{C}(\mathbf{P})$ for each $\mathbf{P}(\mathbf{r}, t)$. The inclusion of an immersed boundary object (consisting here of ~60 points) adds an overhead that, as expected, does not scale with the grid size.

III. RESULTS

Here, we describe several test cases demonstrating the physical features that may be resolved using the simulation methods outlined above. We simulate an optical trap experiment in which an elastic droplet is dragged by a harmonic trap through a viscoelastic fluid over a time T_{pull} and then released. Throughout this section, the main metric we use to evaluate the behavior is the return, which is defined as

$$\text{return} = 1 - d_{ret}/d_{pull}, \tag{42}$$

where d_{ret} is the distance from the lipid droplet's initial center of mass position to its position at the end of the simulation and d_{pull} is the length of the harmonic trap pulling protocol. If the droplet fully returned to its starting position, $d_{ret} = 0$ and return = 1.

The parameters used here are given in Table I. A typical relaxation time for these simulations is $\lambda_1 = 10$ s, and by defining the typical flow rate as $U = d_{pull}/T_{pull}$, the strain rate as $\dot{\gamma} = U/L$, and the observation time as $T = T_{pull}$, we have De = 50, Wi = 40, Re = 0.03, $\beta = 0.98$. For this parameter regime, the system behaves quite elastically and there is significant return of the droplet.

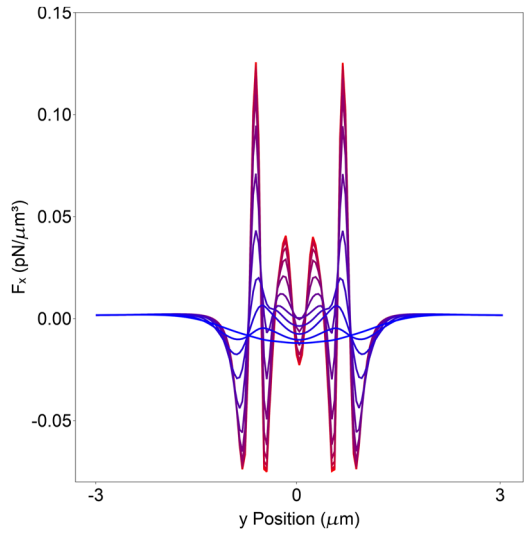

FIG. 8. Effect of stress diffusion on the force distribution. For the values of D_p used in Fig. 6(a), the x-component of $\nabla \cdot \boldsymbol{\sigma}^p$ is visualized at $t = 0.2$ s on the vertical line at $x = 2$ μm passing through the droplet's center of mass. The colors range from red to blue as D_p increases, showing how the force distribution becomes more spatially inhomogeneous for small D_p. For clarity, only part of the full domain $[-5, 5]$ μm has been visualized.

A. Scalar viscoelasticity results

Several parameters entering the simulation setup are shown here to have significant effects on the return. In Fig. 6, we show how the return depends on two such parameters: the droplet radius R and the stress diffusion constant D_p. The range of D_p is consistent in order of magnitude with the measurements made in Ref. 48

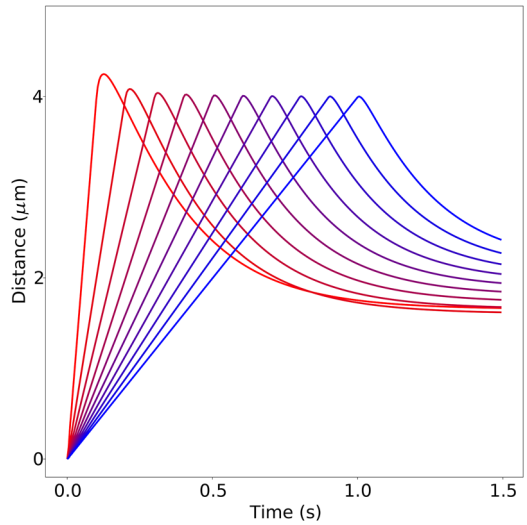

FIG. 9. Distance trajectories for several pulling speeds. The time T_{pull} over which the droplet is pulled corresponds to the point at which each trajectory obtains its maximum (except for the smallest values of T_{pull} which exhibit some overshoot due to convective fluid motion).

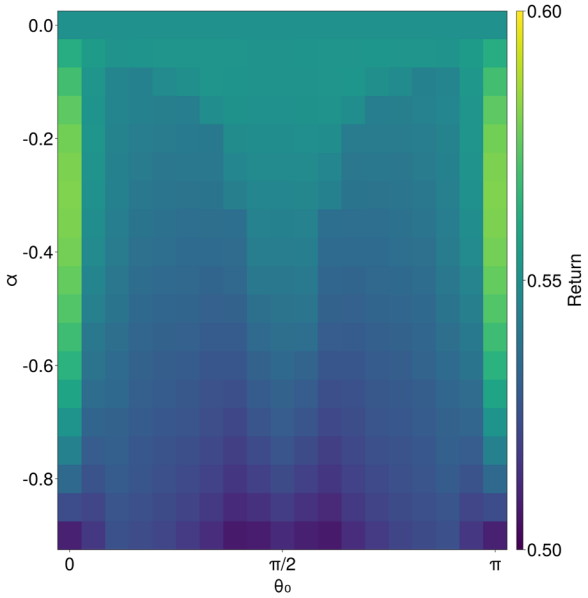

FIG. 10. The value of the return, defined in Eq. (42), as a function of the parameters α, which controls the typical polarization P through $P = \sqrt{-\alpha/\beta}$, and θ_0, the initial angle between the aligned polymer field and the $+x$ direction.

on the viscoelastic stress diffusion in a worm-like micellar solution of CTAB-$NaNO_3$. We observe a non-monotonic dependence of the return on both R and D_p. In the case of D_p [Fig. 6(a)], this non-monotonic dependence can be understood as follows: At very low values of D_p, the viscoelastic restoring force $\nabla \cdot \boldsymbol{\sigma}^p$ has large gradients and is spatially inhomogeneous. In particular, significant components of the restoring force do not align with the direction of return, which diminishes the return. The vector field corresponding to this case is shown in Fig. 7(a) (Multimedia view). On the other hand, when D_p is large, the stress diffuses quickly, which diminishes the magnitude of $\nabla \cdot \boldsymbol{\sigma}^p$ and, in turn, the return; see Fig. 7(c) (Multimedia view). See Fig. 8 for an illustration of these forces as D_p is varied. These competing effects cause the optimal return to occur at intermediate values of D_p. The non-monotonic dependence on the radius [Fig. 6(b)] is a result of a trade-off between higher drag on the droplet and larger elastic displacement of the droplet as the radius increases; see Figs. 7(d)–7(f) (Multimedia view).

In Fig. 9, we show trajectories of the droplet distance as we vary the time T_{pull} over which the droplet is pulled the distance $d_{pull} = 4\ \mu$m. We see that as the droplet is pulled more quickly, it returns closer to its original position. This can be attributed to the reduced amount of time over which the viscous dissipation acts to diminish the viscoelastic restoring force.

B. Tensorial viscoelasticity results

We now illustrate how using a tensorial description of polymer elasticity can produce anisotropy and spatial asymmetry in the viscoelastic restoring forces. The stiffness tensor $\mathbf{C}(\mathbf{P})$ has entries depending on the local polymer polarization vector $\mathbf{P}(\mathbf{r})$, such that both the magnitude of the polarization P and the relative angle between the elastic deformation and the polymer orientation $\hat{\mathbf{P}}$ contribute to the viscoelastic response. To illustrate this, we fix the direction of pulling along the x-axis and vary both the equilibrium polarization P and the initial angle θ_0 that the aligned polymer field makes with this direction. The equilibrium polarization can be found from the free energy [cf. Eq. (16)] as $\sqrt{-\alpha/\beta}$, and we fix $\beta = 1$

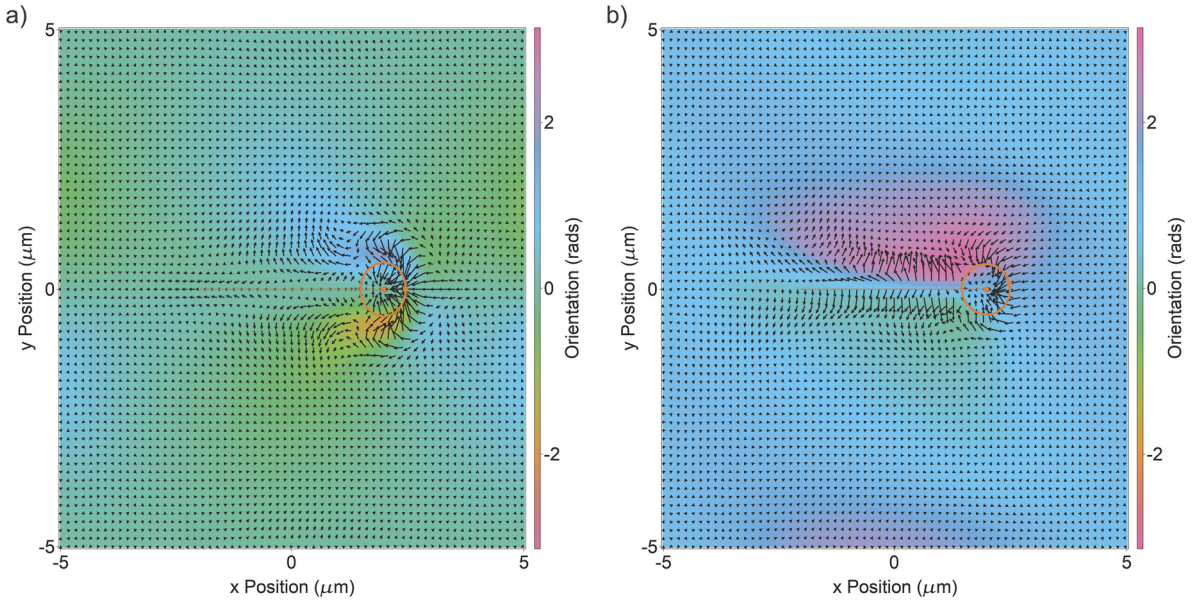

FIG. 11. The orientation field $\mathbf{P}(\mathbf{r})$ at $t = 0.2$ s with initial orientation angle (a) $\theta_0 = 0$ and (b) $\pi/3$; $\alpha = -0.9$. The color indicates the local angle that $\mathbf{P}(\mathbf{r})$ makes with the x-axis, and the arrows are proportional to $\nabla \cdot \boldsymbol{\sigma}^p$. The remaining details of the visualization are the same as in Fig. 7. Note that the tracked point represented by the orange dot on the droplet's boundary has rotated off of the line $y = 0\ \mu$m in panel (b). Multimedia views: (a) https://doi.org/10.1063/5.0123470.1; (b) https://doi.org/10.1063/5.0123470.2

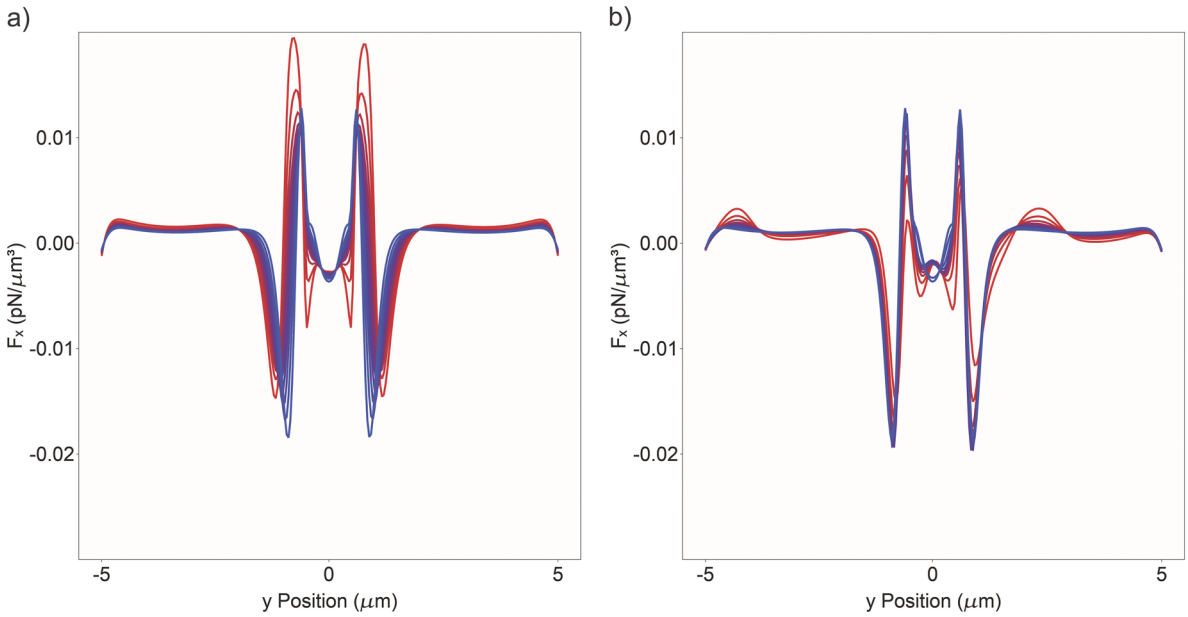

FIG. 12. The x-component of the force density $\nabla \cdot \boldsymbol{\sigma}^{\mathrm{p}}$ on the line $x = 2$ μm for (a) $\theta_0 = 0$ and (b) $\pi/3$ as α ranges from 0 (blue) to −0.9 (red). These plots correspond to the same simulation and time point as shown in Fig. 11. Note that asymmetries about $y = 0$ μm develop for $\theta_0 = \pi/3$ when $\alpha < 0$.

and vary α from 0 to −0.9, causing P to vary from 0 to ~0.95. The return as a function of α and θ_0 is shown in Fig. 10. We see that, as expected, when $\alpha = P = 0$ the system is isotropic [see Eq. (30)] and there is no dependence of the return on θ_0. As P grows, strong dependencies of the return on θ_0 emerge, indicating the onset of anisotropic viscoelastic response. We observe that this anisotropic response, as measured by the return parameter, is periodic with period π and has a reflection symmetry about $\pi/2$.

The fluid flow from the dragged droplet distorts the initially aligned polymer field via the coupling of $\mathbf{P}(\mathbf{r})$ to the velocity gradient tensor [cf. Eq. (15)]. This is visualized in Fig. 11 (Multimedia view) for two initial orientations: $\theta_0 = 0$ and $\pi/3$. For $\theta_0 = 0$, the pulling direction and initial polymer orientation are parallel, and the restoring forces $\nabla \cdot \boldsymbol{\sigma}^{\mathrm{p}}$ are symmetric about the pulling direction. However, this symmetry is broken when $\theta_0 = \pi/3$, and as a result the restoring forces push asymmetrically on the droplet. We observe that this asymmetry causes the droplet to deflect off the axis along which it was pulled as well as to rotate slightly.

We highlight that in the tensorial model, spatial asymmetries of the restoring force that are not captured in the scalar model can now be resolved. This is further illustrated in Fig. 12, where we show the x-component of $\nabla \cdot \boldsymbol{\sigma}^{\mathrm{p}}$ for a range of values of θ_0 and α. For $\theta_0 = 0$, the restoring force is symmetric about $y = 0$ μm for all values of α, while for $\theta_0 = \pi/3$ asymmetries develop as α increases. These unbalanced restoring forces on the top and bottom of the droplet lead to its deflection and rotation as noted above.

IV. DISCUSSION

Our goal in this work was to develop a method for treating fluid structure in hydrodynamic simulations of viscoelastic media. In particular, we introduced a tensorial representation of the elastic modulus $\mathbf{C}(\mathbf{P})$ that depends on the local polarization vector $\mathbf{P}(\mathbf{r})$ of the fluid structure. In the test cases that we presented, this was shown to cause the viscoelastic return of a dragged lipid droplet to become strongly anisotropic. In addition, it was shown that, even in the case that the elastic modulus is a scalar, the viscoelastic return depends non-monotonically on the droplet's size and the diffusion rate of the polymeric stress. We note that, while scalar viscoelasticity has been treated in previous lattice Boltzmann works, we are not aware of any study on the viscoelastic return accompanying a pulled droplet as reported here. Furthermore, the tensorial model of viscoelasticity has not been treated in previous studies. These applications demonstrate the new physical features that the modeling approaches developed in this work can resolve.

Several extensions to the work presented here are possible. First, generalizing these methods to three dimensions rather than two should be straightforward. One difficulty that can arise is analytically evaluating the integral of the parameterized distribution $g(\hat{\mathbf{n}}; k)$ over the unit sphere rather than the unit circle [cf. Eq. (21)]. The choice of $g(\hat{\mathbf{n}})$ here as a von-Mises distribution facilitated computing the stiffness tensor analytically in two dimensions, but computing the stiffness tensor in three dimensions may require resorting to numerical methods. Options for this include precomputing $\mathbf{C}$ on a discretized domain and using a look-up table or a fit of a function to these data or relying on rejection sampling for numerically evaluating the integral. We also note that the expression for the elastic stress tensor can be written in a more general setting as a double integral over a two-body distribution function of polymer orientations rather than as a single integral over a one-body distribution $g(\hat{\mathbf{n}})$ as in Ref. 76. This approach can allow incorporating

domain knowledge of the polymeric system being simulated but will likely complicate the implementation.

Additionally, when the relevant length scales are microscopic, thermal noise may become important. Fluctuations of the fields ρ and $\mathbf{v}$ could be treated using existing variations of the lattice Boltzmann algorithm as discussed in Refs. 53, 77, and 78. Alternative computational fluid dynamics techniques such as stochastic rotation dynamics (also known as multiparticle collision dynamics) could also be considered.[30,79] To a first approximation, thermal noise could be introduced solely through these stochastic methods for solving the Navier–Stokes equation, and the fluctuating $\mathbf{v}$ field would then cause fluctuations in the dynamics of the fields $\mathbf{P}$ and $\boldsymbol{\sigma}^{\mathrm{P}}$ through the dependence of these fields on $\mathbf{v}$. However, a physically rigorous approach for introducing noise consistently in the dynamics of these different fields would likely require further theoretical developments.

A useful generalization of the methods presented here would be to simulate systems with nematic, rather than polar, symmetry. A polar gel, which we considered here, is described by the order parameter $\mathbf{P}$, which we used as the basis for our description of tensorial elasticity. The right-hand side of Eq. (15) is odd under $\hat{\mathbf{P}} \to -\hat{\mathbf{P}}$, but this symmetry for the dynamics of a polar system can be broken by including an even self-advection term $\sim \mathbf{P} \cdot \nabla\mathbf{P}$ in Eq. (15). Such a term can represent, for instance, the directed polymerization of actin polymers.[55,80] We note that the elasticity tensor $\widetilde{\mathbf{C}}(\mathbf{P})$ derived here obeys

$$\widetilde{\mathbf{C}}(\mathbf{P}) = \widetilde{\mathbf{C}}(-\mathbf{P}), \tag{43}$$

which can be seen by observing that the elements $\widetilde{C}_{\alpha\beta}$ (whose expressions are in Appendix B) involve trigonometric functions of even multiples of θ_P. This can be traced to the symmetry $\widetilde{\mathbf{K}}(\hat{\mathbf{n}}) = \widetilde{\mathbf{K}}(-\hat{\mathbf{n}})$, which makes the integral of $\widetilde{\mathbf{K}}$ over the distribution $g(\theta - \theta_P)$ equal to that over $g(\theta - \theta_P - \pi)$. Ultimately, Eq. (43) reflects the assumption of a transversely isotropic material response. Equation (43) enables one to also apply our simulation framework to a nematic gel with an order parameter that is the symmetric and traceless tensor $\mathbf{Q}$.[53,54] The tensor $\mathbf{Q}$ can be expressed in terms of the director $\hat{\mathbf{P}}$ as follows:

$$Q_{ij} = q\left(\hat{P}_i\hat{P}_j - \frac{1}{d}\delta_{ij}\right), \tag{44}$$

where d is the dimensionality and q, like P in the polar case, captures the degree of local alignment. Nematic gels have dynamics given by a variant of the Beris–Edwards equation, summarized in Ref. 53. Importantly, like $\mathbf{C}(\mathbf{P})$, the order parameter $\mathbf{Q}$ is even under $\hat{\mathbf{P}} \to -\hat{\mathbf{P}}$. Adapting the tensorial elastic model presented here to a nematic gel would thus be straightforward: To compute $\widetilde{\mathbf{C}}(\mathbf{Q})$, one could first eigen-decompose $\mathbf{Q}$ to obtain $\hat{\mathbf{P}}$ and q, from which θ_P (modulo π) and the anisotropy parameter k could then be found as in Sec. II C 3 using q in place of P. The integral expression for the elements $\widetilde{C}_{\alpha\beta}$ in Eq. (B1) could then be used directly.

Finally, we neglected here the possibility of activity of the viscoelastic fluid. Activity can allow relaxation of traditional material symmetries, which in turn can give rise to "odd" properties;[57,81] we report simulations of odd viscoelasticity in Ref. 82. Activity can also enable a polymeric network (e.g., the cytoskeleton) to be contractile; such activity can be included in LB simulations by modifying the total stress tensor in the Navier–Stokes equation.[53] In future work, we aim to study the interplay between active stresses and the tensorial viscoelastic restoring forces that are the subject of this paper. It would be interesting to allow the active stresses and elastic stiffness to depend on the local concentration of bound molecular motors in a force-dependent manner, capturing the catch bond-like dynamics of motors such as myosin II.[83] Because feedback loops between the chemistry and mechanics can produce complex energy landscapes, this should lead to a rich dynamical phase diagram with regions in which precise memories of the material's force history can be encoded.

ACKNOWLEDGMENTS

We wish to thank Fred Chang for helpful discussions that motivated the simulations presented. This work was supported by the National Science Foundation through Award Nos. DMR-1848306, EF-1935260, and DMR-2011854. C.F. acknowledges support from the University of Chicago through a Chicago Center for Theoretical Chemistry Fellowship. The authors thank the University of Chicago's Research Computing Center for computing resources.

AUTHOR DECLARATIONS

Conflict of Interest

The authors have no conflicts to disclose.

Author Contributions

Carlos Floyd: Investigation (lead); Writing – original draft (equal). **Suriyanarayanan Vaikuntanathan**: Conceptualization (equal); Funding acquisition (equal); Supervision (equal); Writing – review & editing (equal). **Aaron R. Dinner**: Conceptualization (equal); Funding acquisition (equal); Supervision (equal); Writing – review & editing (equal).

DATA AVAILABILITY

The code implementing this method is available at https://github.com/dinner-group/stave.

APPENDIX A: DETAILS OF THE IMMERSED BOUNDARY METHOD

The IB method was introduced by Peskin to model the interaction of fluids with an elastic boundary.[31,32] The boundary is represented by a set of N_{IB} points $\mathbf{R}_a$ that are not confined to the regular grid of the LB domain but can take any position within the simulation volume. We use the index a to specify points in the IB. In the applications that we present, the points $\mathbf{R}_a$ represent the one-dimensional boundary of a two-dimensional droplet. The elastic properties of the droplet are modeled through a constitutive equation describing the droplet's energy as a function of its configuration as follows:

$$U\left(\{\mathbf{R}_a\}_{a=1}^{N_{IB}}\right) = \sum_{a=1}^{N_{IB}}\left(u_a^{\mathrm{spring}} + u_a^{\mathrm{angle}}\right) + u^{\mathrm{trap}}. \tag{A1}$$

The function u_a^{spring} is a harmonic potential that constrains the separation $l_a = |\mathbf{R}_{a+1} - \mathbf{R}_a|$ between neighboring points to be close to an equilibrium value l_{eq},

$$u_a^{\text{spring}} = \frac{k_{\text{spring}}}{2}(l_a - l_{\text{eq}})^2. \tag{A2}$$

The function u_a^{angle} penalizes regions of high curvature by constraining the angle γ_a between adjacent edges (as drawn in Fig. 13),

$$u_a^{\text{angle}} = \varepsilon_{\text{angle}}(1 - \cos(\pi - \gamma_a)). \tag{A3}$$

To simulate an optical or magnetic trap pulling on the droplet, we add a harmonic potential term constraining the distance between the center of mass $\mathbf{r}_{\text{com}}$ of the points $\{\mathbf{R}_a\}_{a=1}^{N_{IB}}$ and the externally controlled trap position $\mathbf{R}_{\text{ext}}(t)$ as follows:

$$u^{\text{trap}} = \frac{k_{\text{trap}}(t)}{2}|\mathbf{R}_{\text{ext}}(t) - \mathbf{R}_{\text{com}}|^2. \tag{A4}$$

We let both $k_{\text{trap}}(t)$ and $\mathbf{R}_{\text{ext}}(t)$ depend on time so that the trap can be turned on and off as well as moved in space. Figure 13 provides a schematic of the IB model.

The droplet is assumed to be permeable, so that both the exterior and interior of the closed loop contain the fluid. The interaction between the points $\mathbf{R}_a$ and the fluid is bidirectional. In the boundary-to-fluid direction, the constitutive equation $U(\{\mathbf{R}_a\}_{a=1}^{N_{IB}})$ produces forces $\mathbf{f}_a = -\nabla_{\mathbf{R}_a} U$ at the positions $\mathbf{R}_a$. These forces are "spread" to the grid points of the LB domain through kernel-weighted sums over the IB points in the vicinity of the grid points. Different choices of kernels are possible, and in this work we use

$$K(\mathbf{r}) = \phi(r_x)\phi(r_y)/(\Delta x)^2, \tag{A5}$$

where

$$\phi(x) = \begin{cases} \frac{1}{4}\left(1 + \cos\left(\frac{\pi x}{2}\right)\right), & 0 \le |x| \le 2\Delta x, \\ 0, & 2\Delta x \le |x|. \end{cases} \tag{A6}$$

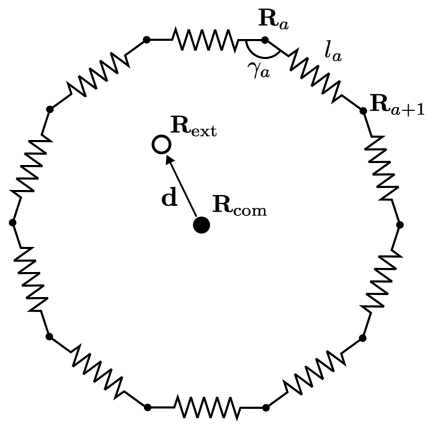

FIG. 13. The N_{IB} points $\mathbf{R}_a$ that make up the immersed boundary are illustrated for $N_{IB} = 10$, showing the quantities l_a, γ_a, $\mathbf{R}_{\text{com}}$, $\mathbf{R}_{\text{ext}}$, and the trap displacement vector $\mathbf{d} = \mathbf{R}_{\text{ext}} - \mathbf{R}_{\text{com}}$ that enter into the constitutive equation for the boundary.

The IB force $\mathbf{f}_{IB}(\mathbf{r})$ at lattice position $\mathbf{r}$ is then computed as

$$\mathbf{f}_{IB}(\mathbf{r}) = \sum_{a=1}^{N_{IB}} \mathbf{f}_a K(\mathbf{R}_a - \mathbf{r}). \tag{A7}$$

For further details on this force-spreading procedure, see Refs. 30, 32, and 37. The force $\mathbf{f}_{IB}$ enters as a contribution toward the external force $\mathbf{f}$ in Eq. (2), which is then accounted for in the LB algorithm following the approach introduced in Ref. 44. In the fluid-to-boundary direction, we assume that there is a no-slip condition between the boundary and the neighboring fluid, such that the boundary points $\mathbf{R}_a$ are simply carried along by the local fluid velocity $\mathbf{v}(\mathbf{R}_a)$. The fluid velocities are only defined on the grid points, so $\mathbf{v}(\mathbf{R}_a)$ is interpolated at the point $\mathbf{R}_a$ using kernel-weighted sums over the lattice points in the vicinity of $\mathbf{R}_a$ as follows:[30]

$$\mathbf{v}(\mathbf{R}_a) = \sum_{\mathbf{r}} (\Delta x)^2 \mathbf{v}(\mathbf{r}) K(\mathbf{R}_a - \mathbf{r}). \tag{A8}$$

For simplicity, we assume here that the boundary motion is overdamped, so that $\partial_t \mathbf{R}_a = \mathbf{v}(\mathbf{R}_a)$. In the time step Δt, the point $\mathbf{R}_a$ is then updated using a finite difference integration scheme in tandem with the LB iteration. We use the predictor–corrector algorithm for all finite difference integration in this paper. It would be straightforward to relax both the no-slip condition, to account for finite friction between the boundary and fluid, and the overdamped condition, to account for inertia of the boundary,[84] but we do not pursue this here.

The pulling protocol, defined by the curves $k_{\text{trap}}(t)$ and $\mathbf{R}_{\text{ext}}(t)$ that enter into Eq. (A4), was observed to lead in some cases to instabilities in the simulation. This occurred when the transitions between resting, pulling, and letting go were not sufficiently smooth, causing high-frequency fluctuations in the fluid. To alleviate this, the pulling protocol is formed from successive sigmoid functions instead of step functions. We use a width of 30 time steps for the sigmoid functions, and before pulling we first let the system equilibrate for 30 time steps.

APPENDIX B: ANISOTROPIC ELASTICITY TENSOR

The expression for the elasticity tensor $\widetilde{\mathbf{C}}(\mathbf{P})$ in the Mandel basis is given by the integral [cf. Eq. (21)]

$$\widetilde{C}_{\alpha\beta}(\theta_P, k; \widetilde{\mathbf{K}}^{\text{x}}) = \int_0^{2\pi} g(\theta - \theta_P; k)\widetilde{K}_{\alpha\beta}(\theta)d\theta, \tag{B1}$$

where θ_P and k are one-to-one functions of P and $\hat{\mathbf{P}}$, $g(\theta;\ k)$ is the von-Mises distribution, and for simplicity we have absorbed the prefactor $(\rho_{\text{p}} - \rho_{\text{ref}})^a$ into the definition of $\widetilde{\mathbf{K}}$. The tensor $\widetilde{\mathbf{K}}(\theta)$ is given as a rotation of the constant tensor $\widetilde{\mathbf{K}}^{\text{x}}$ via Eq. (26), where $\widetilde{\mathbf{K}}^{\text{x}}$ is specified in Eq. (24). The rotation tensor $\widetilde{\mathbf{T}}$ appearing in Eq. (26) is a function of the polar angle θ of $\hat{\mathbf{n}}$, given by

$$\widetilde{\mathbf{T}}(\theta) = \begin{pmatrix} \cos^2\theta & \sin^2\theta & -2\sin\theta\cos\theta \\ \sin^2\theta & \cos^2\theta & 2\sin\theta\cos\theta \\ \sin\theta\cos\theta & -\sin\theta\cos\theta & \cos^2\theta - \sin^2\theta \end{pmatrix}, \tag{B2}$$

and $\widetilde{\mathbf{T}}^{-1}(\theta) = \widetilde{\mathbf{T}}(-\theta)$.

Evaluation of Eq. (B1) gives

$$\widetilde{C}_{11} = \Bigg(\frac{\big(k\big(k^2+24\big)I_0(k) - 8\big(k^2+6\big)I_1(k)\big)\cos(4\theta_P)(K^{\mathrm{x}}_{1111} - 2K^{\mathrm{x}}_{1122} - 4K^{\mathrm{x}}_{1212} + K^{\mathrm{x}}_{2222})}{k^3} + I_0(k)(3K^{\mathrm{x}}_{1111} + 2K^{\mathrm{x}}_{1122} + 4K^{\mathrm{x}}_{1212} + 3K^{\mathrm{x}}_{2222}) + 4I_2(k)(K^{\mathrm{x}}_{1111} - K^{\mathrm{x}}_{2222})\cos(2\theta_P)\Bigg) \Big/ 8I_0(k), \tag{B3}$$

$$\widetilde{C}_{12} = \frac{1}{8}\Bigg(-\frac{\big(k\big(k^2+24\big)I_0(k) - 8\big(k^2+6\big)I_1(k)\big)\cos(4\theta_P)(K^{\mathrm{x}}_{1111} - 2K^{\mathrm{x}}_{1122} - 4K^{\mathrm{x}}_{1212} + K^{\mathrm{x}}_{2222})}{k^3 I_0(k)} + K^{\mathrm{x}}_{1111} + 6K^{\mathrm{x}}_{1122} - 4K^{\mathrm{x}}_{1212} + K^{\mathrm{x}}_{2222}\Bigg), \tag{B4}$$

$$\widetilde{C}_{13} = \Bigg(\frac{\pi\big(k\big(k^2+24\big)I_0(k) - 8\big(k^2+6\big)I_1(k)\big)\sin(4\theta_P)(K^{\mathrm{x}}_{1111} - 2K^{\mathrm{x}}_{1122} - 4K^{\mathrm{x}}_{1212} + K^{\mathrm{x}}_{2222})}{k^3} + 2\pi I_2(k)(K^{\mathrm{x}}_{1111} - K^{\mathrm{x}}_{2222})\sin(2\theta_P)\Bigg) \Big/ 4\pi I_0(k), \tag{B5}$$

$$\widetilde{C}_{21} = \widetilde{C}_{12}, \tag{B6}$$

$$\widetilde{C}_{22} = \widetilde{C}_{11} - \big(I_2(k)(K^{\mathrm{x}}_{1111} - K^{\mathrm{x}}_{2222})\cos(2\theta_P)\big)/I_0(k), \tag{B7}$$

$$\widetilde{C}_{23} = -\Bigg(\frac{\pi\big(k\big(k^2+24\big)I_0(k) - 8\big(k^2+6\big)I_1(k)\big)\sin(4\theta_P)(K^{\mathrm{x}}_{1111} - 2K^{\mathrm{x}}_{1122} - 4K^{\mathrm{x}}_{1212} + K^{\mathrm{x}}_{2222})}{k^3} + 2\pi I_2(k)(K^{\mathrm{x}}_{2222} - K^{\mathrm{x}}_{1111})\sin(2\theta_P)\Bigg) \Big/ 4\pi I_0(k), \tag{B8}$$

$$\widetilde{C}_{31} = \Bigg(\frac{\pi\big(k\big(k^2+24\big)I_0(k) - 8\big(k^2+6\big)I_1(k)\big)\sin(4\theta_P)(K^{\mathrm{x}}_{1111} - 2K^{\mathrm{x}}_{1122} - 4K^{\mathrm{x}}_{1212} + K^{\mathrm{x}}_{2222})}{k^3} + 2\pi I_2(k)(K^{\mathrm{x}}_{1111} - K^{\mathrm{x}}_{2222})\sin(2\theta_P)\Bigg) \Big/ 8\pi I_0(k), \tag{B9}$$

$$\widetilde{C}_{32} = -\Bigg(\frac{\pi\big(k\big(k^2+24\big)I_0(k) - 8\big(k^2+6\big)I_1(k)\big)\sin(4\theta_P)(K^{\mathrm{x}}_{1111} - 2K^{\mathrm{x}}_{1122} - 4K^{\mathrm{x}}_{1212} + K^{\mathrm{x}}_{2222})}{k^3} + 2\pi I_2(k)(K^{\mathrm{x}}_{2222} - K^{\mathrm{x}}_{1111})\sin(2\theta_P)\Bigg) \Big/ 8\pi I_0(k), \tag{B10}$$

$$\widetilde{C}_{33} = \frac{1}{4}\Bigg(-\frac{\big(k\big(k^2+24\big)I_0(k) - 8\big(k^2+6\big)I_1(k)\big)\cos(4\theta_P)(K^{\mathrm{x}}_{1111} - 2K^{\mathrm{x}}_{1122} - 4K^{\mathrm{x}}_{1212} + K^{\mathrm{x}}_{2222})}{k^3 I_0(k)} + K^{\mathrm{x}}_{1111} - 2K^{\mathrm{x}}_{1122} + 4K^{\mathrm{x}}_{1212} + K^{\mathrm{x}}_{2222}\Bigg). \tag{B11}$$

REFERENCES

[1] N. Phan-Thien and N. Mai-Duy, *Understanding Viscoelasticity: An Introduction to Rheology* (Springer, 2013).
[2] R. B. Bird, R. C. Armstrong, and O. Hassager, *Dynamics of Polymeric Liquids, Volume 1: Fluid Mechanics* (John Wiley & Sons, New York, 1987).
[3] D. M. Dykstra, S. Janbaz, and C. Coulais, "The extreme mechanics of viscoelastic metamaterials," *APL Materials* **10**(8), 080702 (2022).
[4] D. Gutierrez-Lemini, *Engineering Viscoelasticity* (Springer, 2014).
[5] R. D. Borcherdt, *Viscoelastic Waves in Layered Media* (Cambridge University Press, 2009).
[6] T. A. Witten and P. A. Pincus, *Structured fluids; Polymers, colloids, surfactants* (Oxford University Press, 2004).
[7] J. D. Paulsen, N. C. Keim, and S. R. Nagel, "Multiple transient memories in experiments on sheared non-Brownian suspensions," Phys. Rev. Lett. **113**, 068301 (2014).
[8] S. Majumdar, L. C. Foucard, A. J. Levine, and M. L. Gardel, "Mechanical hysteresis in actin networks," Soft Matter **14**, 2052–2058 (2018).
[9] D. R. Scheff, S. A. Redford, C. Lorpaiboon, S. Majumdar, A. R. Dinner, and M. L. Gardel, "Actin filament alignment causes mechanical hysteresis in cross-linked networks," Soft Matter **17**, 5499–5507 (2021).

[10]G. Li and A. M. Ardekani, "Collective motion of microorganisms in a viscoelastic fluid," Phys. Rev. Lett. **117**, 118001 (2016).
[11]C. Li, B. Qin, A. Gopinath, P. E. Arratia, B. Thomases, and R. D. Guy, "Flagellar swimming in viscoelastic fluids: Role of fluid elastic stress revealed by simulations based on experimental data," J. R. Soc., Interface **14**, 20170289 (2017).
[12]E. Lauga, "Propulsion in a viscoelastic fluid," Phys. Fluids **19**, 083104 (2007).
[13]G. Li, E. Lauga, and A. M. Ardekani, "Microswimming in viscoelastic fluids," J. Non-Newtonian Fluid Mech. **297**, 104655 (2021).
[14]S. Banerjee, M. L. Gardel, and U. S. Schwarz, "The actin cytoskeleton as an active adaptive material," Annu. Rev. Condens. Matter Phys. **11**, 421–439 (2020).
[15]N. Fakhri, A. D. Wessel, C. Willms, M. Pasquali, D. R. Klopfenstein, F. C. MacKintosh, and C. F. Schmidt, "High-resolution mapping of intracellular fluctuations using carbon nanotubes," Science **344**, 1031–1035 (2014).
[16]E. A. Katrukha, M. Mikhaylova, H. X. van Brakel, P. M. van Bergen En Henegouwen, A. Akhmanova, C. C. Hoogenraad, and L. C. Kapitein, "Probing cytoskeletal modulation of passive and active intracellular dynamics using nanobody-functionalized quantum dots," Nat. Commun. **8**, 14772 (2017).
[17]J. Xie, J. Najafi, R. Le Borgne, J.-M. Verbavatz, C. Durieu, J. Sallé, and N. Minc, "Contribution of cytoplasm viscoelastic properties to mitotic spindle positioning," Proc. Natl. Acad. Sci. U. S. A. **119**, e2115593119 (2022).
[18]J. Najafi, S. Dmitrieff, and N. Minc, "Size and position dependent cytoplasm viscoelasticity through hydrodynamic interactions with the cell surface," bioRxiv:2022.09.27.509722.
[19]F. Amblard, B. Yurke, A. Pargellis, and S. Leibler, "A magnetic manipulator for studying local rheology and micromechanical properties of biological systems," Rev. Sci. Instrum. **67**, 818–827 (1996).
[20]A. R. Bausch, W. Möller, and E. Sackmann, "Measurement of local viscoelasticity and forces in living cells by magnetic tweezers," Biophys. J. **76**, 573–579 (1999).
[21]J. Mas, A. C. Richardson, S. N. S. Reihani, L. B. Oddershede, and K. Berg-Sørensen, "Quantitative determination of optical trapping strength and viscoelastic moduli inside living cells," Phys. Biol. **10**, 046006 (2013).
[22]Y. Jun, S. K. Tripathy, B. R. J. Narayanareddy, M. K. Mattson-Hoss, and S. P. Gross, "Calibration of optical tweezers for *in vivo* force measurements: How do different approaches compare?," Biophys. J. **107**, 1474–1484 (2014).
[23]D. A. Fletcher and R. D. Mullins, "Cell mechanics and the cytoskeleton," Nature **463**, 485–492 (2010).
[24]V. S. Volkov and V. G. Kulichikhin, "On the basic laws of anisotropic viscoelasticity," Rheol. Acta **46**, 1131–1138 (2007).
[25]R. Y. Kwon, A. J. Lew, and C. R. Jacobs, "A microstructurally informed model for the mechanical response of three-dimensional actin networks," Comput. Methods Biomech. Biomed. Eng. **11**, 407–418 (2008).
[26]D. DeKee and R. Chhabra, *Transport Processes in Bubbles, Drops and Particles* (CRC Press, 2002).
[27]Y. L. Raikher, V. V. Rusakov, and R. Perzynski, "Brownian motion in a viscoelastic medium modelled by a Jeffreys fluid," Soft Matter **9**, 10857–10865 (2013).
[28]S. Paul, B. Roy, and A. Banerjee, "Free and confined Brownian motion in viscoelastic Stokes–Oldroyd B fluids," J. Phys.: Condens. Matter **30**, 345101 (2018).
[29]R. Mankin, K. Laas, and N. Lumi, "Memory effects for a trapped Brownian particle in viscoelastic shear flows," Phys. Rev. E **88**, 042142 (2013).
[30]T. Krüger, H. Kusumaatmaja, A. Kuzmin, O. Shardt, G. Silva, and E. M. Viggen, *The Lattice Boltzmann Method: Principles and Practice* (Springer International Publishing, Switzerland, 2017), pp. 4–15.
[31]C. S. Peskin, "Flow patterns around heart valves: A numerical method," J. Comput. Phys. **10**, 252–271 (1972).
[32]C. S. Peskin, "The immersed boundary method," Acta Numer. **11**, 479–517 (2002).
[33]Z.-G. Feng and E. E. Michaelides, "The immersed boundary-lattice Boltzmann method for solving fluid–particles interaction problems," J. Comput. Phys. **195**, 602–628 (2004).
[34]T. Krüger, D. Holmes, and P. V. Coveney, "Deformability-based red blood cell separation in deterministic lateral displacement devices—A simulation study," Biomicrofluidics **8**, 054114 (2014).
[35]X. He and L.-S. Luo, "Theory of the lattice Boltzmann method: From the Boltzmann equation to the lattice Boltzmann equation," Phys. Rev. E **56**, 6811 (1997).
[36]P. J. Dellar, "Bulk and shear viscosities in lattice Boltzmann equations," Phys. Rev. E **64**, 031203 (2001).
[37]S. K. Kang and Y. A. Hassan, "A comparative study of direct-forcing immersed boundary-lattice Boltzmann methods for stationary complex boundaries," Int. J. Numer. Methods Fluids **66**, 1132–1158 (2011).
[38]Y.-H. Qian and Y.-F. Deng, "A lattice BGK model for viscoelastic media," Phys. Rev. Lett. **79**, 2742 (1997).
[39]L. Giraud, D. d'HumièRes, and P. Lallemand, "A lattice-Boltzmann model for visco-elasticity," Int. J. Mod. Phys. C **8**, 805–815 (1997).
[40]J. Ma, Z. Wang, J. Young, J. C. S. Lai, Y. Sui, and F.-B. Tian, "An immersed boundary-lattice Boltzmann method for fluid-structure interaction problems involving viscoelastic fluids and complex geometries," J. Comput. Phys. **415**, 109487 (2020).
[41]I. Ispolatov and M. Grant, "Lattice Boltzmann method for viscoelastic fluids," Phys. Rev. E **65**, 056704 (2002).
[42]O. Malaspinas, N. Fiétier, and M. Deville, "Lattice Boltzmann method for the simulation of viscoelastic fluid flows," J. Non-Newtonian Fluid Mech. **165**, 1637–1653 (2010).
[43]V. Dzanic, C. S. From, and E. Sauret, "A hybrid lattice Boltzmann model for simulating viscoelastic instabilities," Comput. Fluids **235**, 105280 (2022).
[44]Z. Guo, C. Zheng, and B. Shi, "Discrete lattice effects on the forcing term in the lattice Boltzmann method," Phys. Rev. E **65**, 046308 (2002).
[45]R. G. Larson, *Constitutive Equations for Polymer Melts and Solutions* (Butterworth-Heinemann, Stoneham, 2013).
[46]J. G. Oldroyd, "On the formulation of rheological equations of state," Proc. R. Soc. London, Ser. A **200**, 523–541 (1950).
[47]P. D. Olmsted, O. Radulescu, and C.-Y. D. Lu, "Johnson–Segalman model with a diffusion term in cylindrical Couette flow," J. Rheol. **44**, 257–275 (2000).
[48]H. Mohammadigoushki and S. J. Muller, "A flow visualization and superposition rheology study of shear-banding wormlike micelle solutions," Soft Matter **12**, 1051–1061 (2016).
[49]J. Málek, V. Průša, T. Skřivan, and E. Süli, "Thermodynamics of viscoelastic rate-type fluids with stress diffusion," Phys. Fluids **30**, 023101 (2018).
[50]S. Liu, S. Shankar, M. C. Marchetti, and Y. Wu, "Viscoelastic control of spatiotemporal order in bacterial active matter," Nature **590**, 80–84 (2021).
[51]A. Gupta and D. Vincenzi, "Effect of polymer-stress diffusion in the numerical simulation of elastic turbulence," J. Fluid Mech. **870**, 405–418 (2019).
[52]A. Mezrhab, M. Bouzidi, and P. Lallemand, "Hybrid lattice-Boltzmann finite-difference simulation of convective flows," Comput. Fluids **33**, 623–641 (2004).
[53]L. N. Carenza, G. Gonnella, A. Lamura, G. Negro, and A. Tiribocchi, "Lattice Boltzmann methods and active fluids," Eur. Phys. J. E **42**, 81 (2019).
[54]M. C. Marchetti, J. F. Joanny, S. Ramaswamy, T. B. Liverpool, J. Prost, M. Rao, and R. A. Simha, "Hydrodynamics of soft active matter," Rev. Mod. Phys. **85**, 1143 (2013).
[55]E. Tjhung, D. Marenduzzo, and M. E. Cates, "Spontaneous symmetry breaking in active droplets provides a generic route to motility," Proc. Natl. Acad. Sci. U. S. A. **109**, 12381–12386 (2012).
[56]A. N. Beris and B. J. Edwards, *Thermodynamics of Flowing Systems: With Internal Microstructure* (Oxford University Press, New York, 1994).
[57]D. Banerjee, V. Vitelli, F. Jülicher, and P. Surówka, "Active viscoelasticity of odd materials," Phys. Rev. Lett. **126**, 138001 (2021).
[58]F. C. MacKintosh, J. Käs, and P. A. Janmey, "Elasticity of semiflexible biopolymer networks," Phys. Rev. Lett. **75**, 4425 (1995).
[59]C. Storm, J. J. Pastore, F. C. MacKintosh, T. C. Lubensky, and P. A. Janmey, "Nonlinear elasticity in biological gels," Nature **435**, 191–194 (2005).
[60]C. P. Broedersz and F. C. MacKintosh, "Modeling semiflexible polymer networks," Rev. Mod. Phys. **86**, 995 (2014).
[61]J. H. Irving and J. G. Kirkwood, "The statistical mechanical theory of transport processes. IV. The equations of hydrodynamics," J. Chem. Phys. **18**, 817–829 (1950).
[62]W. S. Slaughter, *The Linearized Theory of Elasticity* (Springer Science & Business Media, 2012).

[63]M. Maździarz, "Comment on 'The computational 2D materials database: High-throughput modeling and discovery of atomically thin crystals,'" 2D Mater. **6**, 048001 (2019).
[64]M. Bao, *Analysis and Design Principles of MEMS Devices* (Elsevier, 2005).
[65]G. S. Watson, "Distributions on the circle and sphere," J. Appl. Probab. **19**, 265–280 (1982).
[66]M. Kuron, C. Stewart, J. de Graaf, and C. Holm, "An extensible lattice Boltzmann method for viscoelastic flows: Complex and moving boundaries in Oldroyd-B fluids," Eur. Phys. J. E **44**, 1–14 (2021).
[67]P. R. de Souza Mendes, "Dimensionless non-Newtonian fluid mechanics," J. Non-Newtonian Fluid Mech. **147**, 109–116 (2007).
[68]N. D. Waters and M. J. King, "Unsteady flow of an elastico-viscous liquid," Rheol. Acta **9**, 345–355 (1970).
[69]F. Osmanlic and C. Körner, "Lattice Boltzmann method for Oldroyd-B fluids," Comput. Fluids **124**, 190–196 (2016).
[70]M. E. Cates, K. Stratford, R. Adhikari, P. Stansell, J.-C. Desplat, I. Pagonabarraga, and A. J. Wagner, "Simulating colloid hydrodynamics with lattice Boltzmann methods," J. Phys.: Condens. Matter **16**, S3903 (2004).
[71]K. Wolff, D. Marenduzzo, and M. E. Cates, "Cytoplasmic streaming in plant cells: The role of wall slip," J. R. Soc., Interface **9**, 1398–1408 (2012).
[72]O. Henrich, K. Stratford, D. Marenduzzo, and M. E. Cates, "Ordering dynamics of blue phases entails kinetic stabilization of amorphous networks," Proc. Natl. Acad. Sci. U. S. A. **107**, 13212–13215 (2010).
[73]J. M. Adams, S. M. Fielding, and P. D. Olmsted, "The interplay between boundary conditions and flow geometries in shear banding: Hysteresis, band configurations, and surface transitions," J. Non-Newtonian Fluid Mech. **151**, 101–118 (2008).
[74]T. Markovich, E. Tjhung, and M. E. Cates, "Shear-induced first-order transition in polar liquid crystals," Phys. Rev. Lett. **122**, 088004 (2019).
[75]J. Bezanson, A. Edelman, S. Karpinski, and V. B. Shah, "Julia: A fresh approach to numerical computing," SIAM Rev. **59**, 65–98 (2017).
[76]Z. Liao, M. Han, M. Fruchart, V. Vitelli, and S. Vaikuntanathan, "A mechanism for anomalous transport in chiral active liquids," J. Chem. Phys. **151**, 194108 (2019).
[77]R. Adhikari, K. Stratford, M. E. Cates, and A. J. Wagner, "Fluctuating lattice Boltzmann," Europhys. Lett. **71**, 473 (2005).
[78]B. Dünweg and A. J. Ladd, "Lattice Boltzmann simulations of soft matter systems," in *Advanced Computer Simulation Approaches for Soft Matter Sciences III* (Springer, 2009), p. 89-166.
[79]G. Gompper, T. Ihle, D. Kroll, and R. Winkler, "Multi-particle collision dynamics: A particle-based mesoscale simulation approach to the hydrodynamics of complex fluids," in *Advanced Computer Simulation Approaches for Soft Matter Sciences III* (Springer, 2009), pp. 1-87.
[80]C. Floyd, C. Jarzynski, and G. Papoian, "Low-dimensional manifold of actin polymerization dynamics," New J. Phys. **19**, 125012 (2017).
[81]C. Scheibner, A. Souslov, D. Banerjee, P. Surówka, W. T. M. Irvine, and V. Vitelli, "Odd elasticity," Nat. Phys. **16**, 475–480 (2020).
[82]C. Floyd, A. R. Dinner, and S. Vaikuntanathan, "Signatures of odd dynamics in viscoelastic systems: From spatiotemporal pattern formation to odd rheology," arXiv:2210.01159 (2022).
[83]W. E. Thomas, V. Vogel, and E. Sokurenko, "Biophysics of catch bonds," Annu. Rev. Biophys. **37**, 399–416 (2008).
[84]M. Bušík, M. Slavík, and I. Cimrák, "Dissipative coupling of fluid and immersed objects for modelling of cells in flow," Comput. Math. Methods Med. **2018**, 7842857.
[85]E. Süli and D. F. Mayers, *An Introduction to Numerical Analysis* (Cambridge University Press, 2003).